Promoting syngas production from steam reforming of toluene using a highly stable Ni/(Mg, Al)O$_x$ catalyst

Jie Ren [a,*], Yi-Ling Liu [b]

[a] *Institute for Technical and Macromolecular Chemistry, RWTH Aachen University, Worringerweg 2, Aachen 52074, Germany*
[b] *Key Laboratory of Coal Processing and Efficient Utilization of Ministry of Education, China University of Mining and Technology, Daxue road 1, Xuzhou 221116, PR China*

ARTICLE INFO

ABSTRACT

Toluene, as one of the representative biomass tar model compound, has been widely chosen for investigation of biomass tar reforming. Herein, novel Ni/(Mg, Al)O$_x$ (Ni/MAO) catalysts derived from Ni-Mg-Al hydrotalcites were prepared successfully and used for steam reforming of toluene (SRT). Among all the catalysts, Ni/MAO catalyst prepared at pH of 10 and aging temperature of 20 °C (Ni/MAO-10) exhibited superior activity in toluene conversion (95.3%) and syngas production (833 mmol/g-Ni), as well as the excellent resistance to carbon deposition. Through characterizations, the highest basicity, highest reducibility, tailored "rosette-like" morphology, and larger specific surface area in Ni/MAO-10 were confirmed. Furthermore, the structure-activity relationship, reforming mechanism, deactivation, and regeneration of the catalyst were comprehensively elaborated from rigorous experiments, and meanwhile, the activation energies and turnover frequency (TOF) values of four Ni/MAO catalysts in SRT were calculated to theoretically explain their activities.

1. Introduction

The excessive utilization of traditional energy caused a series of environmental problems and the crisis of fossil fuels. In recent years, many researchers are struggling to find alternative resources to alleviate this situation [1]. In terms of renewable energy, biomass energy is considered to be a promising resource for liquid, gas, and solid chemical production through thermochemical conversion [2]. Among them, syngas can be produced from biomass gasification and further for chemical production via Fischer-Tropsch synthesis, which therefore gained more attention in industry and academia [3]. However, tar formation during biomass gasification is the most critical obstacle, which can cause serious pollution to equipment, resulting in a decrease in the gasification efficiency [4]. The catalytic removal of biomass tar has proved to be the most efficient method, which could simultaneously obtain H$_2$-rich gas. Nevertheless, in view of the complexity of the tar, toluene, benzene, and naphthalene are usually selected as tar model compounds for mechanism investigations and catalyst design [5–7].

Among the catalysts used, Ni-based catalysts with the cheap price and high catalytic activity are the most commonly used for reforming tar and tar model compounds [8]. Herein, many efforts have been made for support chosen and catalyst fabrication through various synthetic methods. A variety of supports have been selected for Ni-based catalyst preparation and exhibited high activity in reforming of biomass tar and tar model compounds, such as natural minerals, metal oxides, and chars [9–11]. The mentioned supports with different properties like acidity, basicity, and oxygen defects have been proved to be possible for altering products composition. For instance, acidic supports such as Al$_2$O$_3$ are widely used in tar reforming due to their low cost and high surface area, but deactivation of Ni/Al$_2$O$_3$ is inevitable due to the coke formation [12]. Increasing the basicity of the catalyst is essential and beneficial to minimize side reactions during the tar reforming. The presence of basic sites can enhance the non-oxidative cleavage of the C-H bond, and then adsorbed CO$_2$ on the basic site could promote coke elimination and CO formation [13]. Recently, layered double hydroxides with a classical formula of $[M^{2+}_{1-x}M^{3+}_x(OH)_2](A^{n-})_{x/n} \cdot mH_2O$ have attracted increasing attention for catalyst preparation in various topics [14,15]. Mg-Al hydrotalcite, a classical layered double hydroxide, with the general formula of Mg$_6$Al$_2$CO$_3$(OH)$_{16} \cdot 4$ H$_2$O is a well-established support in different reforming reactions [16]. The controllable basicity of the Mg-Al hydrotalcite makes it possible for producing more H$_2$-rich gas, which showed an excellent capacity of CO$_2$ adsorption and reaction with carbon deposition during tar reforming. In particular, the partial substitution of Mg or Al with M^{2+} and M^{3+} ions can tun the physiochemical properties of Mg-Al hydrotalcite. Based on these, Ni-based catalysts are

* Corresponding author.
  E-mail addresses: renchemie@hotmail.com, jie.ren@rwth-aachen.de (J. Ren).

Nomenclature

CO_2-TPD	CO_2 temperature-programmed decomposition
D_{pore}	average pore diameter
DRIFTS	diffuse reflectance infrared Fourier transform spectroscopy
GHSV	gas hourly space velocity
H_2-TPR	H_2 temperature-programmed reduction
HAADF-STEM	high-angle annular dark-field scanning transmission electron microscope
ICP-OES	inductively coupled plasma optical emission spectrometry
MSA	metal surface area
MSI	metal-support interaction
Ni/MAO	Ni supported on $(Mg, Al)O_X$
Ni/MAO-9	Ni/MAO derived from NMAO-9
Ni/MAO-10	Ni/MAO derived from NMAO-10
Ni/MAO-150	Ni/MAO derived from NMAO-150
Ni/MAO-E	Ni/MAO derived from NMAO-E

NCS	Ni crystallite size
NMAO	Ni-Mg-Al oxides
NMAO-9	NMAO prepared under pH= 9 and 20 °C aging
NMAO-10	NMAO prepared under pH= 10 and 20 °C aging
NMAO-150	NMAO prepared under pH= 10 and 150 °C aging
NMAO-E	NMAO prepared under pH= 10 with ethanol and 20 °C aging
RD	reduction degree
S_{BET}	specific surface area
SEM	scanning electron microscope
SRT	steam reforming of toluene
TEM	transmission electron microscope
TOF	turnover frequency
V_{pore}	total pore volume
WGSR	water-gas shift reaction
XRD	X-ray diffraction

frequently synthesized by supporting Ni on Mg-Al hydrotalcite through impregnation and partial substitution of Mg-Al hydrotalcite with Ni during preparation. For instance, Josuinkas et al. [17] obtained partial substitution of Mg-Al hydrotalcite with Ni by the co-precipitation method and successfully applied it for reforming of tar model compounds (i.e., toluene, benzene, and naphthalene) at high temperature. We previously designed Mg-Al hydrotalcites using co-precipitation, and it is found that pH value of the solution is important to obtain wonderful support with great physiochemical properties [18]. However, the morphology of the support was destroyed after Ni addition by impregnation, and the literature already reported that impregnation is not suitable for obtaining the Ni-based catalyst with high Ni loading (i.e., 20 wt% in our previous work). As usual, the catalysts with high Ni loading prepared by the impregnation method are characterized by low Ni dispersion, large crystal size, and low active metal area. Moreover, although literature studies have screened many Ni-based catalysts for syngas production from steam reforming of toluene (SRT), the mechanism for SRT is still limited. Hence, it is important to prepare a highly dispersed Ni-based Mg-Al hydrotalcite and investigate its activity in syngas production from toluene reforming. Besides, understanding the

structure-activity relationship of Ni-based catalysts under harsh conditions is crucial for the development of gasification technology.

In this paper, $Ni/(Mg, Al)O_x$ (Ni/MAO) catalysts derived from Ni-Mg-Al hydrotalcites were prepared by coprecipitation, calcination and reduction, and then catalysts with different morphologies were applied for SRT. Effects of reaction temperature and S/C ratio on gas production and toluene conversion were investigated for activity evaluation. Especially, the stability of the catalyst was evaluated in detail by the method of intermittent steam supply. Through different characterization techniques, the structure-activity relationship and mechanism of toluene cracking were concluded to explain the influence of catalyst preparation on the catalyst properties and activity in SRT.

2. Experimental section

2.1. Materials preparation

As shown in Fig. 1a, the Ni-Mg-Al hydrotalcites were fabricated by co-precipitation of $Ni(NO_3)_2 \cdot 6H_2O$, $Mg(NO_3)_2 \cdot 6H_2O$ and $Al(NO_3)_3 \cdot 9H_2O$ with the (Ni+Mg)/Al ratio of 3/1 at 80 °C. Briefly, the solution
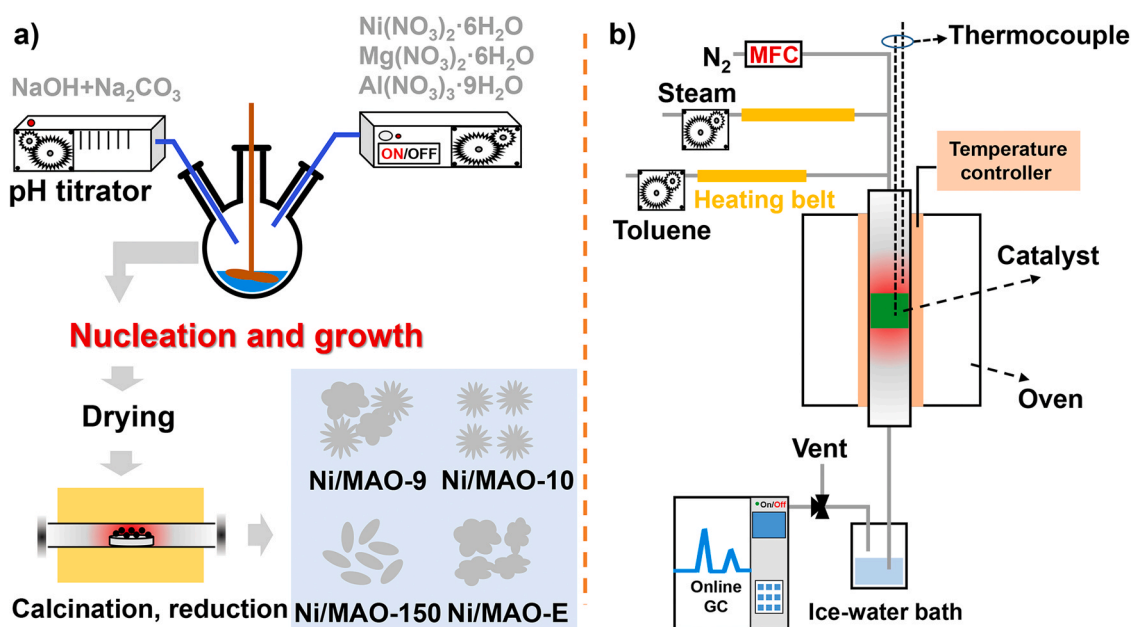

Fig. 1. Schematic diagram of catalyst preparation (a) and reforming setup (b).

contains NaOH and Na_2CO_3 was used to adjust solution pH, and then obtained precipitates were aged for 20 h. After that, the obtained precipitates were washed with deionized water and dried at 100 °C for 15 h. Finally, dried Ni-Mg-Al hydrotalcites were ground to 0.5–1 mm and calcined at 500 °C for 3 h under an air atmosphere. The obtained Ni-Mg-Al oxides (NMAO) were reduced at 600 °C for 2 h before being applied for SRT and characterization, and the catalysts were named Ni/MAO.

Here, the NMAO derived from Ni-Mg-Al hydrotalcites prepared at pH of 9 and 10 (aged temperature: 20 °C) were named NMAO-9 and NMAO-10. NMAO derived from Ni-Mg-Al hydrotalcite prepared at pH of 10 (aged temperature: 150 °C) was named as NMAO-150, and NMAO derived from Ni-Mg-Al hydrotalcite prepared at pH of 10 (aged temperature: 20 °C) but solution contains a certain amount of ethanol during co-precipitation was denoted as NMAO-E. The corresponding Ni/MAO catalysts derived from the reduction treatment of NMAO were named Ni/MAO-9, Ni/MAO-10, Ni/MAO-150, Ni/MAO-E, respectively. The contents of Ni, Mg, and Al in the obtained Ni/MAO catalyst were determined by inductively coupled plasma optical emission spectrometry (ICP-OES).

2.2. Apparatus and procedures

Nitrogen physisorption was measured using a Quantachrome Autosorb-1 instrument at − 196 °C. In brief, around 100 mg Ni/MAO catalysts were evacuated to 0.3 mbar at 300 °C for 6 h before the measurement. The specific surface area (S_{BET}) of the sample was calculated using the Brunauer–Emmett–Teller method from Quantachrome software. The total pore volume (V_{pore}) of the sample was calculated at a relative pressure (P/P_0) of 0.95. X-ray diffraction (XRD) patterns of the samples were recorded using a Bruker D8 Advance with Cu-Kα radiation at 45 kV and 40 mA, and the scanned 2θ angle was varied from 10° to 90°. ICP-OES was conducted using a Thermo Fisher Scientific iCAP 6300 with a photomultiplier tube detector, and the samples were dissolved in *aqua regia* for 12 h before the analysis. A JEOL JXA-8530 F scanning electron microscope (SEM) equipped with an energy dispersive X-ray spectroscopy (EDX) detector was employed to observe the morphology of the Ni/MAO catalysts. Ni particle size and distribution of Ni/MAO catalysts were characterized using a FEI Tecnai F20 transmission electron microscope (TEM) equipped with EDX and a high-angle annular dark-field (HAADF) detector, which operated at an acceleration potential of 200 kV. CO_2 temperature-programmed decomposition (CO_2-TPD), H_2 temperature-programmed reduction (H_2-TPR), and CO pulse chemisorption were conducted in a Micromeritics Autochem II 2920 machine equipped with a thermal conductivity detector. For H_2-TPR, about 100 mg of NMAO samples were put into a U-shaped quartz reactor and treated with a higher temperature (150 °C) to remove the water. Subsequently, the TPR profiles were monitored by a thermal conductivity detector from room temperature to 1000 °C. The reduction degree (RD) of the catalysts was calculated using the following equation:

$$RD\ (\%) = \frac{\text{TPR area of calcined sample-TPR area of reduced sample}}{\text{TPR area of calcined sample}}$$
$$\times 100\% \qquad (1)$$

For CO_2-TPD, about 150 mg of NMAO samples were loaded into a U-shaped quartz reactor and first reduced in-situ under 5% H_2/Ar (50 mL/min) at 600 °C for 2 h and then introducing pure Ar to remove the surface H species of the catalysts. After that, the temperature was decreased to 50 °C to adsorb CO_2 (50 mL/min of 5% CO_2 diluted in He for 1 h) and then desorb physisorbed CO_2 by 50 mL/min He for 1 h. Finally, the CO_2 desorption curves of the samples were recorded by mass spectrometer from 50 °C to 900 °C. In-situ diffuse reflectance infrared Fourier transform spectroscopy (DRIFTS) measurements were performed at a Bruker Vertex 70 spectrometer, and the NMAO samples were put into an in-situ high-temperature cell (Harrick Praying Mantis).

Before the measurement, the catalyst was first reduced at 600 °C for 2 h, and then the background spectra were recorded at room temperature under 20 mL/min N_2 atmosphere. During the measurement, the 0.05 mL/min toluene and water (S/C= 0, 1, and 2) were introduced into the cell through bubbling, and 64 scans were recorded for each spectrum with the spectral resolution of 4 cm^{-1}.

2.3. Reforming experiments

The SRT was performed in a self-designed fixed bed system, which equipped including a quartz tube (i.d. 1.0 cm), mass flow controller (MFC), HPLC pump, and online gas chromatography (Fig. 1b). 200 mg of NMAO diluted in inert SiC (1800 mg) was first in-situ reduced with 50 mL/min H_2 at 600 °C for 2 h. After that, the steam and toluene were evaporated through the heating belt (set at 150 °C), and then toluene (1.5 mL/h) and steam (S/C = 0–4) together with N_2 as the carrier gas were injected into the system from the top using HPLC pumps and MFC with a total gas hourly space velocity (GHSV) of 5000 h^{-1}. Finally, the gaseous product and residual toluene were determined by a Shimadzu GC-2014 online gas chromatograph (pass through a water trap to absorb excessive steam and organic products), which was equipped with a thermal conductivity detector and a flame ionization detector. All the SRT experiments were performed three times, and data were adapted when the performance was stable. In addition, to have accurate results, blank experiments were performed in the presence of inert SiC. The toluene conversion (X) was calculated by the following equations:

$$X(\%) = \frac{n[CO]_{out} + n[CO_2]_{out} + n[CH_4]_{out}}{7n[Toluene]_{in}} \qquad (2)$$

Turnover frequency (TOF) (h^{-1}) of toluene conversion was calculated as follows:

$$TOF\ (h^{-1}) = \frac{1.5 \times 0.866 \times X \times 58.69}{92.14 \times 0.2 \times D_{Ni} \times L_{Ni}} \qquad (3)$$

where $n[CO]_{out}$, $n[CO_2]_{out}$, and $n[CH_4]_{out}$ are the molar flow rate of output CO, CO_2, and CH_4; and $n[Toluene]_{in}$ is the molar flow rate of input toluene; L_{Ni} and D_{Ni} are Ni loading and Ni dispersion, respectively. 1.5, 0.866, 58.69, 92.14, and 0.2 represent the flow rate of toluene, the density of toluene, molar mass of Ni, molar mass of toluene, and mass of catalyst, respectively.

3. Results and discussion

3.1. Materials characterizations

3.1.1. Textural analysis of materials

According to the International Union of Pure and Applied Chemistry (IUPAC) classification [19], all Ni/MAO catalysts are belonging to type II isotherms as shown in Fig. 2a. This kind of isotherm represents the unrestricted monolayer-multilayer adsorption and the existence of spaces between the layers. As can be seen from Fig. 2a, desorption immediately starts for all Ni/MAO catalysts and following a type H4 hysteresis loop for the samples aged at 20 °C. Moreover, the hysteresis loop of all catalysts aged at room temperature (i.e., Ni/MAO-9, Ni/MAO-10, and Ni/MAO-E) closed at a relative pressure of around 0.4, which proved the existence of a broad pore size distribution of the mesopores of them. For the Ni/MAO-150 (i.e., aged at 150 °C for 24 h), it possessed a classical type H3 hysteresis loop, which indicated the formation of a plate-like structure with slit-shaped pores [20].

S_{BET}, V_{pore}, and average pore diameter (D_{pore}) of the obtained Ni/MAO catalysts were calculated from software and concluded in Table 1. Ni/MAO-10 and Ni/MAO-E presented the highest S_{BET} (131.2 and 145.9 m^2/g) while Ni/MAO-150 showed the lowest S_{BET} (94.5 m^2/g) among these catalysts. Considering the D_{pore} and V_{pore} of all samples, four catalysts showed different D_{pore} values but the different contents of
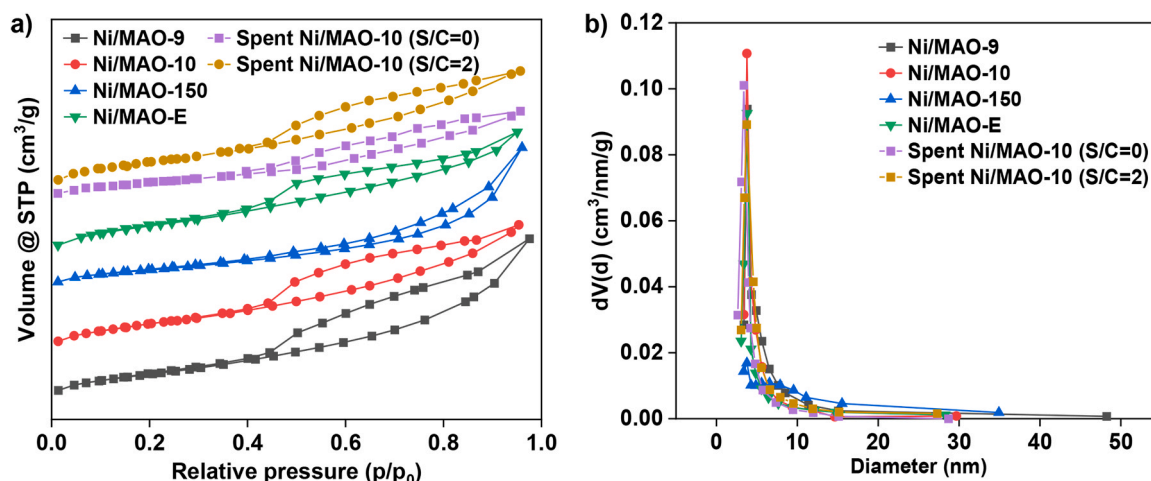
Fig. 2. Nitrogen physisorption isotherms (a) and pore size distribution (b) of the synthesized Ni/MAO catalysts and spent Ni/MAO-10 under different conditions.

Table 1
Textural properties of the Ni/MAO catalysts.

	NCS (nm)	S_{BET} (m²/g)	V_{pore} (cm³/g)	D_{pore} (nm)	RD (%)
Ni/MAO-9	7.1	124.5	0.22	7.19	88.6
Ni/MAO-10	6.5	131.2	0.18	5.51	92.3
Ni/MAO-150	7.5	94.5	0.19	8.24	87.2
Ni/MAO-E	6.9	145.9	0.18	4.95	90.7
Spent Ni/MAO-10(S/C=0)	–	97.9	0.10	4.97	–
Spent Ni/MAO-10 (S/C=2)	–	128.1	0.17	5.32	–
Commer. Ni/Al₂O₃	10.1	121.1	0.21	10.4	89.1

the mesopores led to a similar in V_{pore} among the catalysts. In consistent with particle size distribution (Fig. 2b), the results evidenced that Ni/MAO-150 holds bigger mesopores but lower V_{pore} than other Ni/MAO catalysts, verifying fewer pore contents were inside the catalysts. Generally, the difference in textural properties of the synthesized catalysts plays a crucial role in Ni dispersion and distribution. In comparison with our previous work, the Ni/(Mg, Al)O$_x$ prepared through Ni-Mg-Al hydrotalcites possessed the larger S_{BET}, which may exhibit higher activity in SRT due to increased accommodation of highly dispersed Ni.

3.1.2. XRD analysis of materials

XRD patterns of the Ni-Mg-Al hydrotalcites and Ni/MAO catalysts were shown in Fig. 3. All the Ni-Mg-Al hydrotalcites presented strong reflections with (003) and (006) diffraction peaks at 11.6 and 23.1° indicating the formation of classical Ni-Mg-Al hydrotalcite crystal structure. There has no other phase that can be found in Fig. 3a, indicating the high purity of the obtained Ni-Mg-Al hydrotalcites. Interestingly, the Ni-Mg-Al hydrotalcite prepared under pH of 10 and aging at 150 °C (i.e., Ni/MAO-150 catalyst precursor) showed higher than the other three Ni/MAO catalyst precursors in both the peak density and peak area, indicating the higher crystallinity of the Ni/MAO-150 catalyst precursor. Ni/MAO-10 catalyst precursor exhibited a similar peak shape and intensity with Ni/MAO-E catalyst precursor, which demonstrated the similar crystal structure of these two materials. After calcination and reduction, metallic Ni species were obviously crystallized in all four Ni/MAO catalysts (Fig. 3b). For instance, the diffraction peaks at 2θ of 37.0°, 44.5°, 62.5°, 75.0°, and 78.9° were attributed to (111), (200), and (220) crystal planes of metallic Ni phases (JCPDS No. 45-1027). In addition to metallic Ni, the existed NiO should be the uncomplete reduction of the catalysts or the rapid oxidation during the sample transfer. A further explanation about the Ni state will be found in the H₂-TPR and XPS analysis in the following sections. Furthermore, the possible species like MgO, Al₂O₃ and MgAl₂O₄ in Ni/MAO catalysts cannot be detected, indicating the high uniformity of supports. As mentioned in previous literature, metal crystallite size of the catalyst has a decisive influence on the activity in tar reforming, and the catalyst with low metal crystallite size usually processes a high active surface-to-volume ratio. The Ni crystallite size (NCS) of all catalysts were
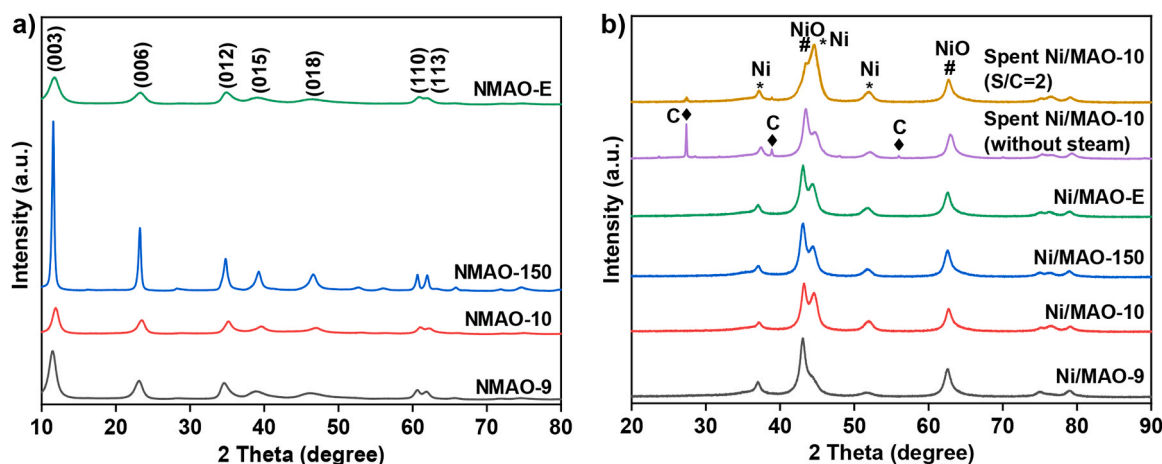

Fig. 3. XRD patterns of obtained Ni-Mg-Al hydrotalcites (a), Ni/MAO catalysts and spent Ni/MAO-10 catalysts (b).

calculated by Scherrer formula (D = Kγ/Bcosθ) and were 7.1, 6.5, 7.5, and 6.9 nm for Ni/MAO-9, Ni/MAO-10, Ni/MAO-150, and Ni/MAO-E, respectively, suggesting that Ni/MAO-10 and Ni/MAO-E with the lower NCS may have higher activity in SRT.

3.1.3. H₂-TPR and CO₂-TPD analysis

To observe the reduction behavior and reduction degree (RD) of the NMAO, H_2-TPR profiles were recorded from room temperature to 1000 °C under H_2 atmosphere (Fig. S1, Supporting Information). The obtained NMAO samples exhibited two reduction peaks in the temperature range, that is, the lower temperature peak (400–490 °C) and a higher temperature peak at 850–900 °C, which denoted the reduction of surface NiO and the reduction of NiO species with stronger interaction with support. Among these samples, the H_2-TPR profiles of NMAO-9 and NMAO-10 possessed the lower reduction temperature peaks located at approximately 485 °C. However, in comparison to NMAO-9 (i.e., maximum temperature at 895 °C), the maximum temperature for the NMAO-10 was lower (i.e., 879 °C), indicating the weaker metal-support interaction (MSI) of NMAO-10 [21]. It indicated that the difference in pH value during co-precipitation may lead to different structures for NMAO-9 and NMAO-10 catalysts. Similar to NMAO-9 and NMAO-10, the existence of weak MSI in NMAO-E also showed two reduction peaks at temperatures centered at 450 and 872 °C. In contrast to NMAO-9, NMAO-10, and NMAO-E, the NMAO-150 presented three reduction peaks (i.e., α −, β −, and γ − Ni) at approximately 415, 525, and 895 °C, which could be potentially assigned to the different MSIs. In addition, the RD of all the catalysts were calculated using relative area, and the results (Table 1) showed the catalysts possessed 88.6%, 92.3%, 87.2%, and 90.7% for Ni/MAO-9, Ni/MAO-10, Ni/MAO-150, and Ni/MAO-E, respectively. Therefore, in comparison to Ni-based hydrotalcite-derived catalysts obtained by incipient wetness impregnation previously, the prepared NMAO samples herein using the co-precipitation could possess the higher NiO dispersion and easily be reduced at 600 °C. Usually, the apparent differences observed in the H_2-TPR curves can be attributed to the different adsorption and interaction of the active metal Ni with different morphologies in catalysts during the preparation.

According to the literature, Ni-based MgAl hydrotalcite-derived catalysts usually exhibited superior basic properties, which may be advantageous for the adsorption of gas (e.g., CO_2) and acidic reactants [22, 23]. Thus, CO_2-TPD was employed to investigate the total basicity and basic site distribution of the Ni/MAO catalysts. The desorption of CO_2 was monitored in a temperature range of 50–900 °C (Fig. 4). As shown in Fig. 4, CO_2-TPD profiles of all catalysts were mathematically deconvoluted into three Gaussian peaks, which could attribute to weak, medium, and strong basic sites at 50–200 °C, 200–500 °C, and 500–900 °C, respectively. In general, the catalyst with high basicity may be helpful to activate steam, decrease the deposited carbon, and then enhance the toluene conversion on the surface of the catalyst during SRT reaction. For instance, Ashok et al. [24] found the $La_{0.8}Ce_{0.2}Co_{0.5}Ti_{0.5}O_{3-\delta}$ with the higher basicity showed higher toluene conversion, anti-H_2S, and anti-NO_x activity during SRT.

Herein, the week, medium, and strong basic sites of Ni/MAO catalysts were quantified and correlated to their activity in SRT. The contents of total basic sites and basic site distribution were determined by the area of CO_2-TPD and summarized in Table 2. The total basicity of the four catalysts follow the order: Ni/MAO-10 > Ni/MAO-E > Ni/MAO-9 > Ni/MAO-150. Among the obtained catalysts, the Ni/MAO-10 possessed a higher amount of basic sites (1.56 mmol/g), while Ni/MAO-150 exhibited lower basic sites (0.99 mmol/g). Through the calculations of basic sites distribution, it was observed that Ni/MAO-10 had weak, medium, and strong basic sites of 0.46 mmol/g_{cat}, 0.94 mmol/g_{cat}, and 0.16 mmol/g_{cat}, respectively, suggesting this catalyst with the high and uniform basicity would provide excellent activity in SRT afterward. Moreover, Ni/MAO-150 possessed lower basicity and concentrated medium basic sites, which might have worse catalytic
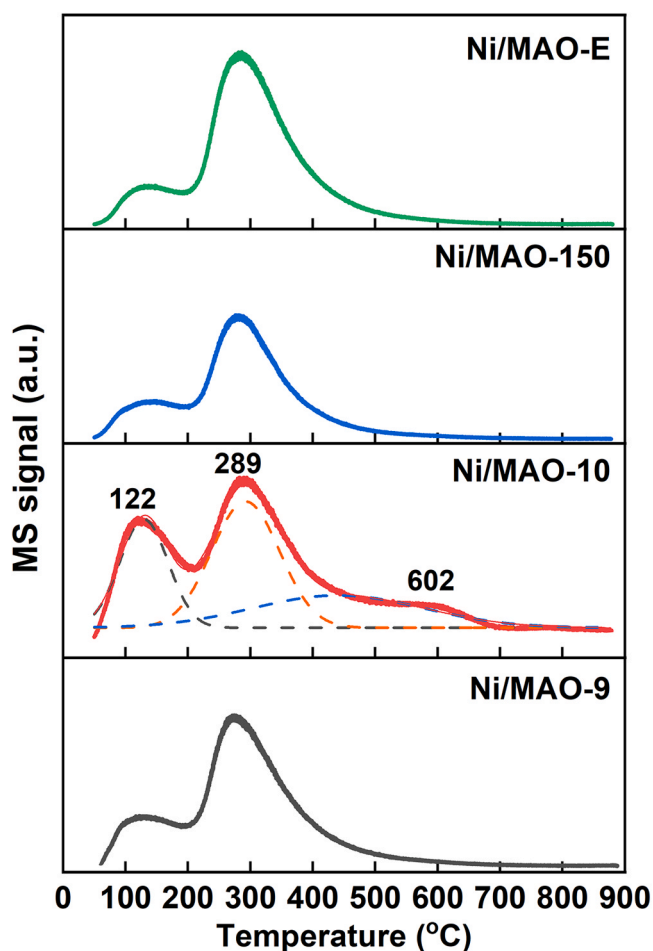

Fig. 4. CO_2-TPD profiles of synthesized Ni/MAO catalysts.

Table 2
Basic site distribution and TOF value of Ni/MAO catalysts prepared under different conditions.

Catalyst	Total basic sites (mmol/g_{cat})	Basic sites distribution (mmol/g_{cat})			TOF (h^{-1})
		Weak	Medium	Strong	
Ni/MAO-9	1.19	0.15	0.96	0.08	2.26
Ni/MAO-10	1.56	0.46	0.94	0.16	2.79
Ni/MAO-150	0.99	0.15	0.79	0.05	2.00
Ni/MAO-E	1.37	0.25	1.11	0.01	2.70

performance in the reforming of toluene.

3.1.4. SEM and TEM analysis

The morphologies and Ni particle size distribution of the synthesized Ni/MAO catalysts prepared under different conditions were characterized by SEM and TEM. As depicted in Fig. 5, the various treatment used in Ni/MAO catalyst preparation led to the formation of different morphologies. The SEM images revealed that Ni/MAO-9 and Ni/MAO-10 have a similar "rosette-like" morphology, but the slightly structural modification when the pH increased from 9 to 10 during co-precipitation. As reported in the literature [25], the competitive precipitation of Ni^{2+}, Mg^{2+}, Al^{3+}, the formation of $Ni_{1-x}Mg_xAl-A$ (A represents HCO_3^- or CO_3^{2-} here), and the preferential growth of (Ni, Mg)₃Al-CO₃ along with the 001 planes are the formation mechanism for "rosette-like" morphology of Ni/MAO-10 (see Fig. S2, Supporting Information). In comparison with the catalyst prepared before [18], the
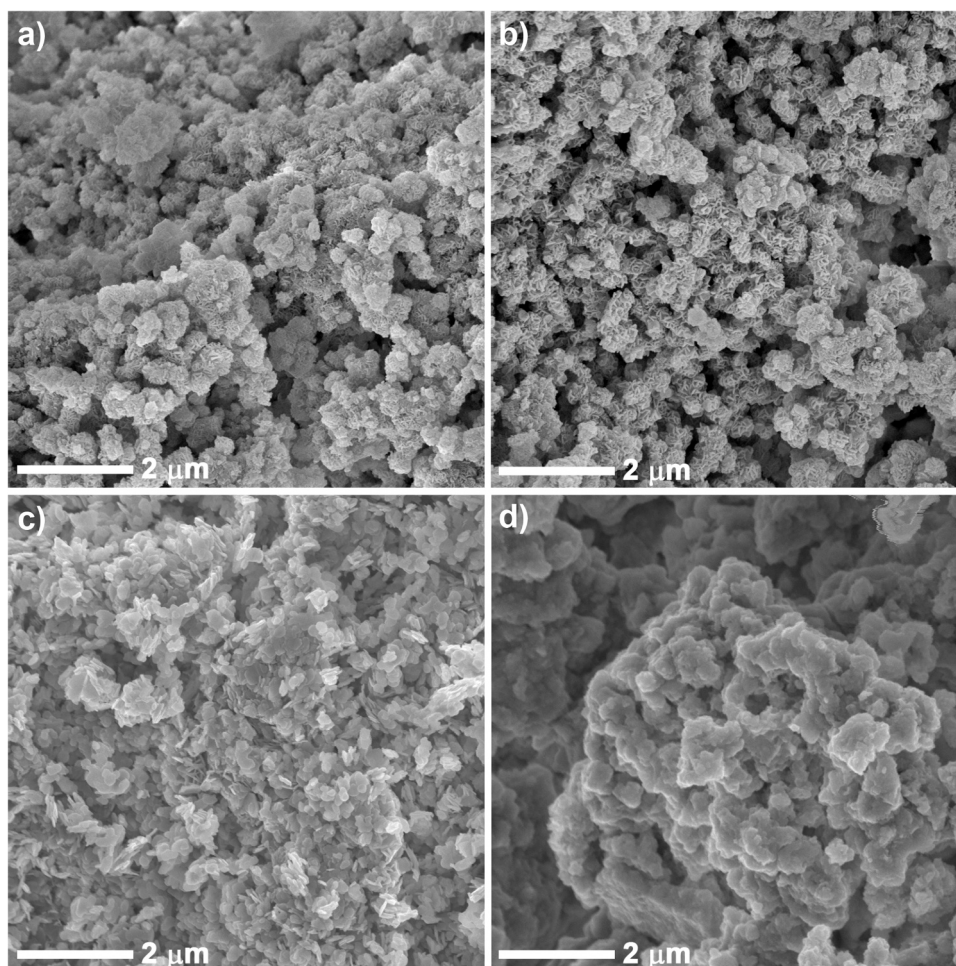
Fig. 5. SEM images of different Ni/MAO catalysts (Ni/MAO-9 (a), Ni/MAO-10 (b), Ni/MAO-150 (c), and Ni/MAO-E (d), respectively).

morphology of the catalyst prepared herein can be well retained and the Ni addition during hydrotalcite preparation cannot affect the nucleation and growth of the hydrotalcite. Ni/MAO-150 prepared under hydrothermal treatment at higher temperature caused a formation of hexagonal "plate-like" structure, which belonged to highly crystalline material. About Ni/MAO-E, the petals of the rosette structure were destroyed and become widen, which led to the formation of a loosely porous structure. Consequently, the existence of a loose porous characteristic observed in Ni/MAO-E might provide enough space and therefore more active sites for the adsorption and reaction of gas and toluene. Moreover, in consistent with the textural properties of the Ni/MAO catalysts (Section 3.1.1), Ni/MAO-150 and Ni/MAO-9 with fewer pores may be less active than the Ni/MAO-10 and Ni/MAO-E. The EDX semi-quantitative results verified the existence and the content of Ni, Mg, Al, and O in all catalysts, which were in agreement with those determined by ICP-OES (i.e., 18.2, 18.9, 17.8, and 19.1 wt% of Ni for Ni/MAO-9, Ni/MAO-10, Ni/MAO-150, and Ni/MAO-E, respectively).

As seen from Fig. 6, metallic Ni particles, visible as dark grains, were uniformly dispersed on the surface of the catalyst. The particle size distribution of four catalysts was also presented in Fig. 6, and it was clearer to observe the distribution of Ni species as expected. In comparison with the other three catalysts and the catalysts in Ref. [18], the Ni/MAO-10 possessed the smallest Ni particle size (3.3 nm) and excellent Ni dispersion. Compared with the results of XRD analysis, the difference in particle size confirms that Ni particles may be partially embedded in the carrier. As reported in the literature, the small particle size may favor the appearance of stronger MSIs, increasing the reduction temperature of the catalyst. Indeed, from the H_2-TPR, the higher

reduction temperature of $\beta - Ni$ was detected for the Ni/MAO-10 catalyst, which is consistent with the smallest Ni metallic particle sizes among the catalyst. In comparison with traditional TEM, HAADF scanning-TEM (HAADF-STEM) uses electron scattering at high angles to create a Z-contrast image with Z denoting the atomic number [26]. Therefore, the heavy elements (i.e., Ni) will be highlighted, and the bright area in Fig. 6e confirmed the high reduction degree of the Ni/MAO-10 (in agreement with the H_2-TPR and XRD analysis). The EDX mapping in the dark area of HAADF-STEM image was recorded and dispersed Ni and O elements were also observed. As reported in the literature, the Ni(111) plane observed in HR-TEM image (Fig. 6f) is thought to be highly active for hydrogenation and reforming reaction, and therefore could exhibit high activity for toluene reforming [6,27, 28]. An inter-planar spacing of 0.203 nm was attributed to Ni(111) planes in metallic Ni particles, which is consistent with XRD analysis in Section 3.1.2. Meanwhile, it also proved that O elements observed in the EDX mapping should come from the support rather than NiO. As a result, Ni/MAO-10 with the better Ni dispersion, smallest Ni particle size, and abundant Ni(111) crystal planes may have higher activity in SRT.

Based on the characterization results, Ni/MAO catalysts derived from Ni-Mg-Al hydrotalcite possessed various pore structures and morphologies. The various morphologies of catalysts were formed when they were aged for 20 h under different conditions after nucleation, growth, and calcination. For instance, Ni/MAO-9 and Ni/MAO-10 showed the rosette-like structure while Ni/MAO-150 aged at 150 °C had a morphology of plate-like structure. Among all the catalysts, Ni/MAO-10 with more pores, wide pore distribution (5–10 nm), and low NCS was expected to accommodate more dispersed Ni, which was also
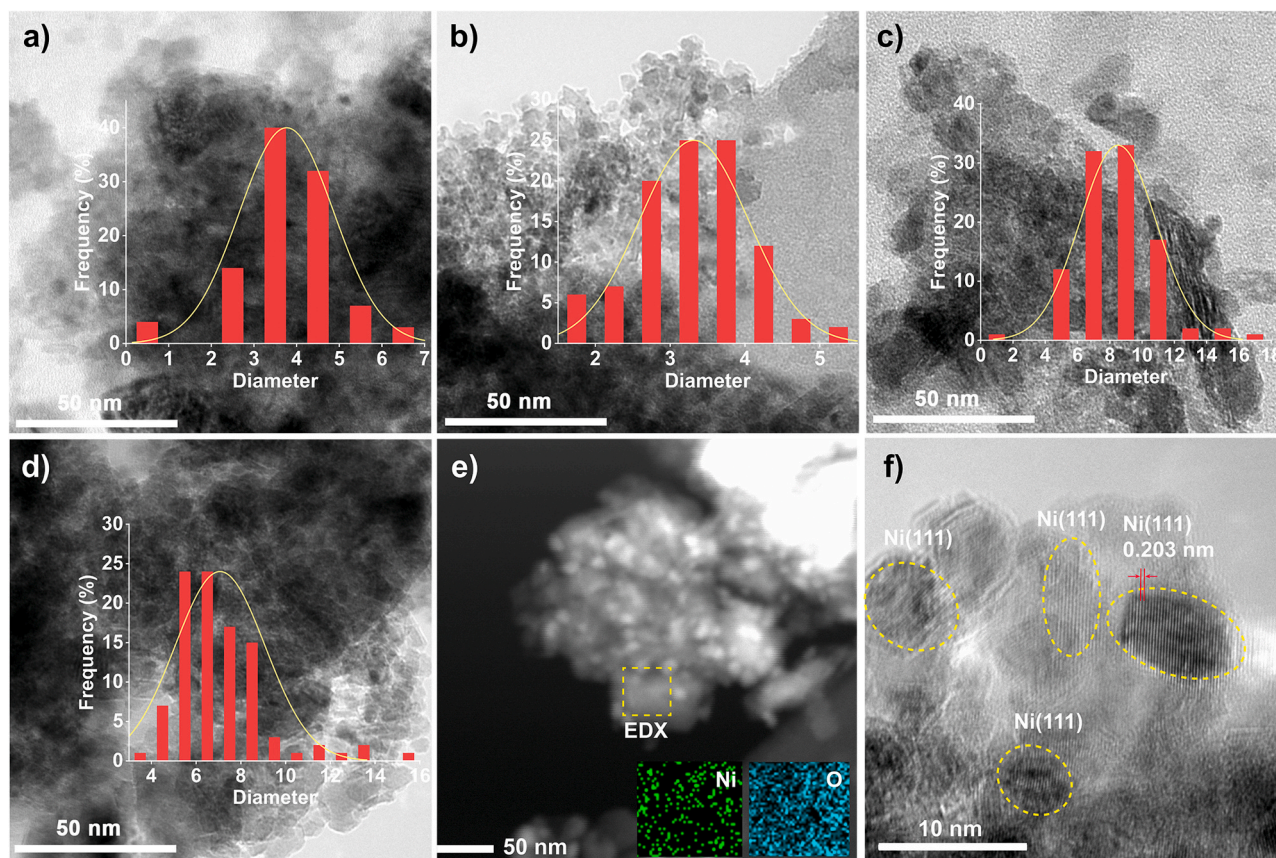
Fig. 6. TEM images of different Ni/MAO catalysts (Ni/MAO-9 (a), Ni/MAO-10 (b), Ni/MAO-150 (c), and Ni/MAO-E (d), respectively); HAADF-STEM (BF mode) image (insert: EDX mapping of Ni and O) (e) and HR-TEM image (f) of Ni/MAO-10 catalyst.

confirmed by SEM and TEM analyses. Combining the findings of H_2-TPR, CO_2-TPD, and CO pulse chemisorption, the excellent properties (i.e., weaker MSIs, higher content of basicity, larger metal surface, and metal dispersion) of Ni/MAO-10 presents a promising catalyst for high toluene conversion in SRT.

3.2. Activity of Ni/MAO catalysts in SRT

3.2.1. Effect of reaction temperature

The influences of reforming temperature on toluene conversion and

syngas yield were studied under conditions of S/C= 2 and a GHSV of 5000 h^{-1}. To eliminate the influence of temperature on the thermal cracking of toluene, the SRT over inert SiC (as a blank experiment) was performed at 400–600 °C. As can be seen from Fig. S3 (Supporting Information), high temperature is required for toluene conversion and more gas release. As reported in the literature, high toluene conversion and gas production from radical collision usually occurs at > 800 °C [29]. Therefore, a small amount of gas release with temperature increase should be the result of coke elimination, water gas reaction, and water-gas shift reaction (WGSR) occurring under steam atmosphere.
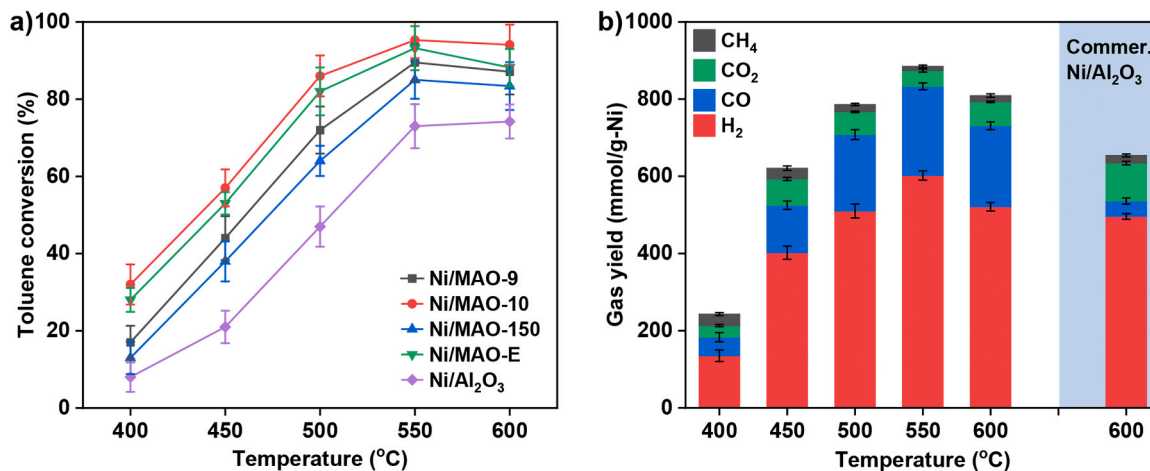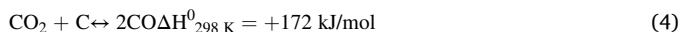

Fig. 7. Toluene conversion over Ni/MAO catalysts and commercial Ni/Al$_2$O$_3$ catalyst at 400–600 °C (a); gas distribution of SRT over Ni/MAO-10 at 400–600 °C and gas distribution of SRT over commercial Ni/Al$_2$O$_3$ at 600 °C (b).

Besides, all of the gas yield and toluene conversion obtained in this work should be subtracted by the thermal cracking of toluene.
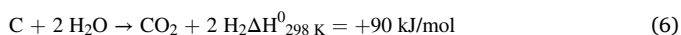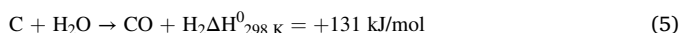
In order to comprehensively compare the activities of the synthesized catalysts, the SRT over Ni/MAO catalysts was conducted and the results were presented in Fig. 7a. With the temperature increasing from 400 to 550 °C, the toluene conversion over all Ni/MAO catalysts was continuously increased. In particular, Ni/MAO-10 exhibited better activity than other catalysts throughout the whole temperature range, and the toluene conversion was increased from 32.0% to 95.3% from 400 to 550 °C.

As reported in the literature [30], steam reforming reaction is endothermic, and therefore a high reaction temperature is beneficial to hydrocarbons decomposition and oxidation of carbon species (Eqs. 4–6) [30,31].

Boudouard reaction:

$$CO_2 + C \leftrightarrow 2CO \quad \Delta H^0_{298\ K} = +172\ kJ/mol \tag{4}$$

Water gas reaction:

$$C + H_2O \rightarrow CO + H_2 \quad \Delta H^0_{298\ K} = +131\ kJ/mol \tag{5}$$

$$C + 2\ H_2O \rightarrow CO_2 + 2\ H_2 \quad \Delta H^0_{298\ K} = +90\ kJ/mol \tag{6}$$

The activity of the catalyst is worse at low temperature, which is not active for the cracking of toluene, while the higher temperature can significantly promote the reforming of toluene into synthetic gas. It is worthy to mention that all Ni/MAO catalysts showed the highest activity at 550 °C while 600 °C is the optimum reforming temperature of Ni/Al$_2$O$_3$ for toluene conversion. The activity of Ni/MAO catalysts follows the order Ni/MAO-10 > Ni/MAO-E > Ni/MAO-9 > Ni/MAO-150 > commercial Ni/Al$_2$O$_3$. For comparison, the catalytic activity of supported Ni-based catalysts from the literature is listed in Table S1 (see Supporting Information). The literature results revealed that the obtained Ni/MAO-10 in this work is the most active catalyst in toluene reforming (95.3% at 550 °C) at a relatively low temperature.

The main gaseous products over Ni/MAO-10 from SRT are H$_2$ followed by CO, CO$_2$, and traces of CH$_4$ as shown in Fig. 7b. The syngas yield increased with an increase of temperature from 400° to 550°C while CO$_2$ yield was fluctuated with the temperature increasing, indicating CO$_2$ might participate in the reaction through the Boudouard reaction. The CO$_2$ yield decreased to the lowest (41.2 mmol/g-Ni) at 550 °C proven that 550 °C was suitable to realize the highest toluene conversion. The extra CO was mainly produced from coke elimination in addition to toluene cracking, which could timely react with carbon deposition and maintain the stability of Ni/MAO-10 catalyst. The deposited carbon can encapsulate Ni particles and cover the active sites of the catalyst, and then resulting in the deactivation of the catalyst. The CH$_4$ yield was significantly decreased from 400 to 600 °C, indicating the reverse methanation of CO/CO$_2$ (CH$_4$ + 2 H$_2$O → CO$_2$ + 4 H$_2$ and CH$_4$ + H$_2$O → CO + 3 H$_2$) became the dominant reaction [32]. Methanation is an exothermic and thermodynamically limited reaction, and the optimum temperature for CH$_4$ production over Ni-based catalysts is 300–400 °C. In this case, a higher temperature (i.e., above 400 °C) will result in a decrease in CH$_4$ yield. In addition, the catalytic performance of commercial Ni/Al$_2$O$_3$ for SRT was also evaluated at 400–600 °C. As illustrated in Fig. S4 in Supporting Information, the tendency of gas yield over commercial Ni/Al$_2$O$_3$ catalysts was monotone increasing with temperature until 600 °C while Ni/MAO-10 showed the maximum toluene conversion and gas yield at 550 °C. Besides, CO$_2$ was the dominant carbon-containing gas product when using commercial Ni/Al$_2$O$_3$ for SRT. As suggested before [33], unlike Ni/MAO-10, Ni/Al$_2$O$_3$ possessed weak basicity cannot enhance CO$_2$ adsorption and subsequent reaction, which hence produced more CO$_2$ and H$_2$ during the whole temperature range. More CO$_2$ can be produced from WGSR, which therefore resulted in a noticeable decrease in CO yield. The syngas yield and toluene conversion over commercial Ni/Al$_2$O$_3$ were

503.2 mmol/g-Ni and 74.2% at 600 °C, which proved the designed Ni/MAO catalysts were the potential to realize toluene conversion at relatively low temperature. To have a fair comparison of gas distribution over Ni/MAO catalysts and commercial Ni/Al$_2$O$_3$, the SRT over commercial Ni/Al$_2$O$_3$ and other Ni/MAO catalysts was carried out under the same conditions (i.e., GHSV = 5000 h^{-1}, S/C=2, and reforming temperature = 550 °C).

As seen from Fig. 8a, in comparison to Ni/MAO catalysts prepared using different supports, commercial Ni/Al$_2$O$_3$ catalyst showed the lowest gas production (654.2 mmol/g-Ni). Surprisingly, commercial Ni/Al$_2$O$_3$ catalyst exhibited higher production of H$_2$ and CO$_2$ under current conditions, and a low amount of CO and CH$_4$ could also be observed. It indicates that the occurrence of WGS (CO + H$_2$O → CO$_2$ + H$_2$) over Ni/Al$_2$O$_3$ catalyst is more favorable [34], and more CO$_2$ can also be produced from the reaction between coke and steam [35]. Consistent with the discussion in the characterization section, the Ni/MAO-150 with the worst properties (e.g., basicity, S$_{BET}$, and reducibility) exhibited less gas production (668.3 mmol/g-Ni) than others. Ni/MAO-E with similar characteristics has a toluene conversion close to that of Ni/MAO-10. Considering the ratio of H$_2$/CO in the gaseous products from SRT, all Ni/MAO catalysts with a relatively optimum H$_2$/CO ratio (2.60 – 4.61) are considered to be suitable for the synthesis of value-added chemicals via Fischer-Tropsch synthesis or other conversion technologies [36,37]. In contrast, the produced gas with the highest H$_2$/CO ratio (12.4) over commercial Ni/Al$_2$O$_3$ cannot be directly used for chemical production [38], and additional removal of the high fraction of CO$_2$ should be considered. In addition, literature studies have proved that commercial Ni/Al$_2$O$_3$ is easily be deactivated by carbon deposition [39–41], and therefore Ni/MAO catalysts prepared in this work deserve to be studied in depth.

3.2.2. Effect of S/C ratio

As mentioned before, the reaction between steam and deposited carbon could promote the production of more syngas and enhanced the stability of the Ni/MAO catalysts. Therefore, the effect of S/C ratio on SRT over tailored Ni/MAO catalysts was evaluated and results were presented in Figs. 8b and 9. In the case of S/C = 0, the toluene conversion over Ni/MAO-9, Ni/MAO-10, Ni/MAO-150, Ni/MAO-E, and commercial Ni/Al$_2$O$_3$ was continuously decreased during 10 h TOS test. The toluene conversion over Ni/MAO-10 decreased from 53.2% to 23.2% after 10 h measurement. Due to the absence of the oxygen source (H$_2$O, O$_2$, or CO$_2$), the deactivation of all Ni/MAO catalysts can be observed during the reforming process. Although the S/C molar ratio was only 1.0, the catalytic activity of all Ni/MAO catalysts was obviously improved. Toluene conversion over Ni/MAO-10 achieved 80%, in consistent with discussed before, the activity of Ni/MAO-10 is the highest among the Ni/MAO catalysts. This indicated that WGSR, water gas reaction, and the reaction (C$_7$H$_8$ + 7 H$_2$O → 7CO + 11 H$_2$) became dominant at this ratio (S/C=1), which promoted the formation of syngas. After further increasing the S/C ratio (S/C=2), the toluene conversion over all Ni/MAO catalysts was again enhanced (Fig. 8b). It demonstrated that the reaction (C$_7$H$_8$ + 14 H$_2$O → 7CO$_2$ + 18 H$_2$) taken place to produce more H$_2$. Here, carbon deposition can be quickly removed through Boudouard reaction and water-gas reaction, this suggested the more H$_2$ and CO were observed in the discussion of Section 3.2.1. However, the toluene conversion was slightly decreased when S/C molar ratio was higher than 2.0. It indicated that the adsorption of steam on the surface of the catalyst was saturated, which led to the activity decreasing of Ni/MAO catalysts in SRT [42]. In the case of S/C= 3.0, the toluene conversion over Ni/MAO-10 was slightly decreased from 93.2% to 89.0% compared with S/C of 2. The yield of H$_2$, CO, CO$_2$, and CH$_4$ also showed a certain decrease, while H$_2$/CO ratio was strengthened when the steam fraction was again increased. However, an excessive steam introduction would take plenty of heat away, and thus leads to energy consumption and reduction of toluene conversion. The same findings were also confirmed by Gao et al. [43] and Zou et al. [30], who found
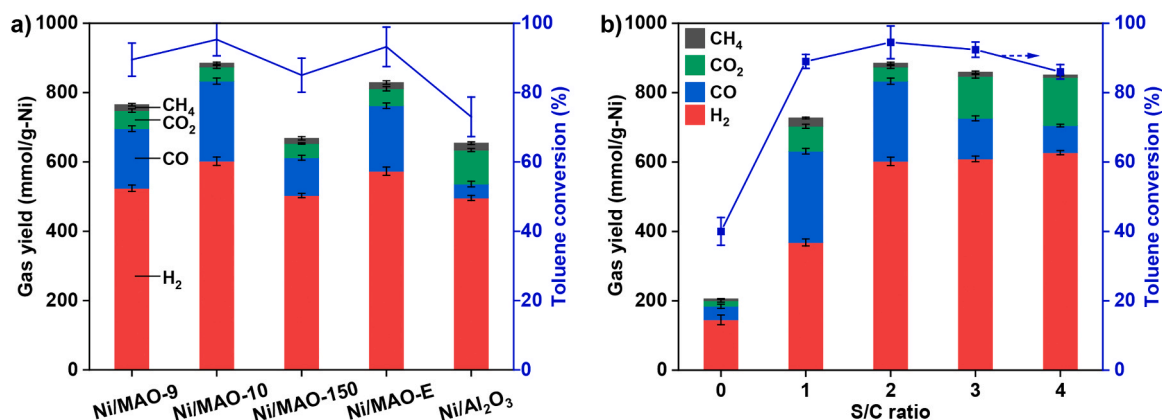
Fig. 8. Toluene conversion and gas yield over Ni/MAO catalysts and commercial Ni/Al$_2$O$_3$ at 550 °C (S/C = 2) (a) and effect of S/C ratio on gas distribution and toluene conversion over Ni/MAO-10 catalyst (b).
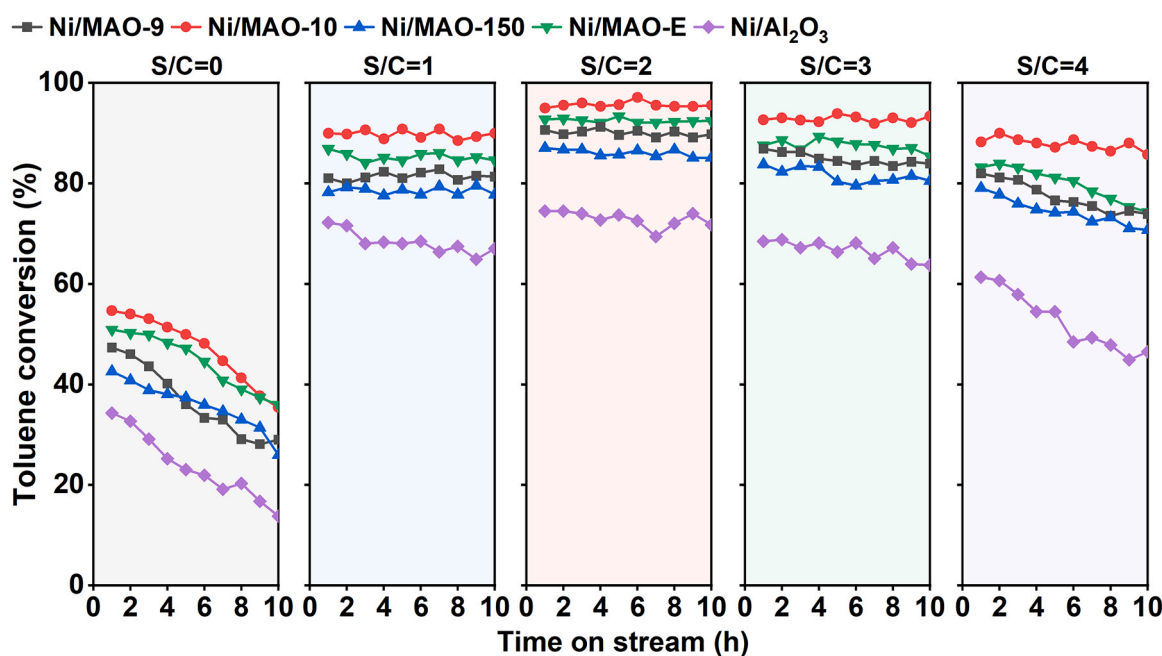

Fig. 9. Effect of S/C ratios on toluene conversion over different Ni/MAO catalysts. Reaction conditions: reforming temperature = 550 °C, 200 mg catalyst, GHSV = 5000 h^{-1}.

that a high S/C molar ratio caused an inverse effect on the catalytic performance of the catalyst in SRT. As the same, the activity of the catalysts prepared herein exhibited a further decrease when an S/C ratio was increased to 4. It should be noted that commercial Ni/Al$_2$O$_3$ catalyst showed unstable activity under different S/C ratios during all tests compared with the Ni/MAO catalysts. Overall, a high S/C molar ratio is not advised from a practical standpoint due to the modification of active sites, cost of gas-liquid separation, and additional energy inputs for steam generation. As a result, in our test scenario, S/C = 2 was recommended as the optimal ratio.

3.3. Stability of Ni/MAO-10 catalyst in SRT

As discussed above, the Ni/MAO-10 exhibited excellent activity and stability for toluene conversion among the Ni/MAO catalysts, which can endure higher steam fraction even up to S/C = 4. Therefore, the steam (with S/C=2) was intermittently injected into the reactor to study the deactivation behavior of the Ni/MAO-10 catalyst during SRT, and the experimental results were depicted in Fig. 10.

The toluene conversion was gradually decreased when non-steam was introduced, and the gas production showed the same trends. During the first running, the decomposition of toluene was mainly the process of thermal cracking. Thus, serious carbon deposition would generate and deposit on the surface of the catalyst to suppress the activity of the Ni/MAO-10 catalyst for toluene conversion. As stated in literature [40,42], the steam introduction is crucial to crack biomass tar/tar model compounds, and the catalyst is easily deactivated by carbon deposition in the absence of steam. Hence, the syngas yield was decreased from 196.2 mmol/g-Ni to 128.1 mmol/g-Ni during 5 h TOS, especially H$_2$ decreased by approximately 34%. After introducing steam (S/C = 2.0) into the system, the activity of Ni/MAO-10 for SRT was obviously regenerated due to coke elimination (Eqs. 5 and 6). As shown in Fig. 10, the toluene conversion significantly increased from 35.4% to 94.9% when the steam was immediately poured into the reactor. In comparison with the first run (without steam), the high yield and fraction of H$_2$ and CO are probably generated from the water gas reaction, suggesting the carbon deposition should be responsible for unexpected activity in toluene conversion under an inert atmosphere. The syngas
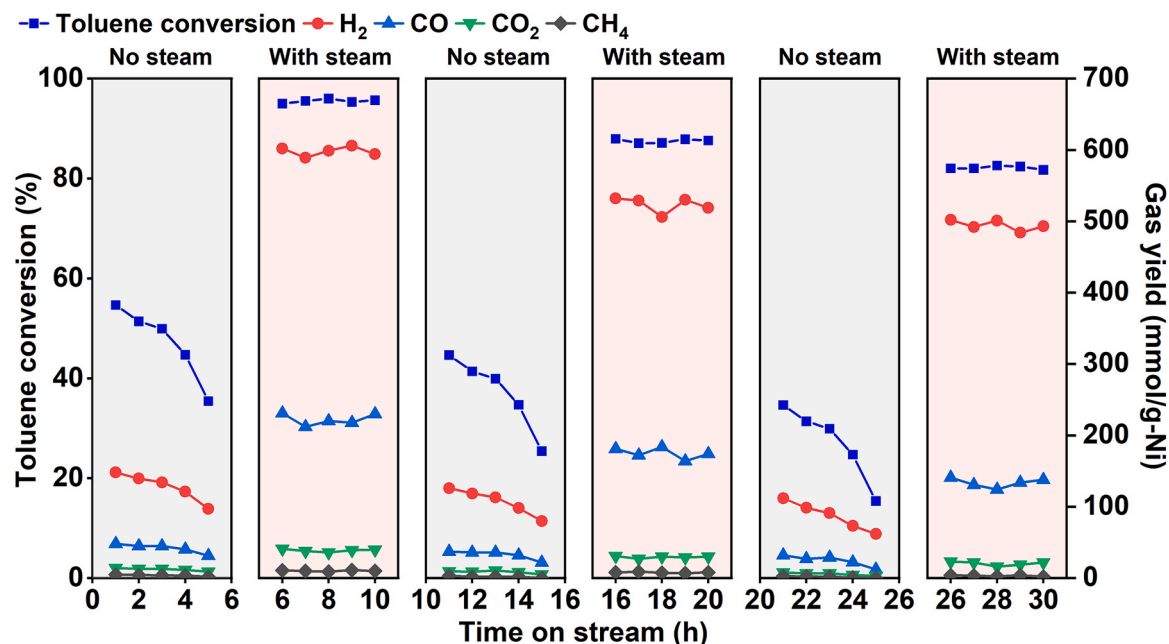
Fig. 10. Intermittent deactivation and regeneration of Ni/MAO-10 catalyst during SRT. Reaction conditions: reforming temperature = 550 °C, S/C = 2.0, 200 mg catalyst, GHSV = 5000 h^{-1}.

production increased sharply from 128.1 mmol/g-Ni to 833.0 mmol/g-Ni while H$_2$/CO evidently improved, indicating the activity regeneration of the Ni/MAO-10 catalyst. The toluene conversion and the yield of H$_2$, CO, CO$_2$, CH$_4$ yields were rapidly backed into the level of first running when steam was ceased (third running). However, the reforming activity over Ni/MAO-10 was not the same as the initial reforming (first running), indicating the activity of the catalyst was not fully recovered during 5 h measurement under steam. The reduced
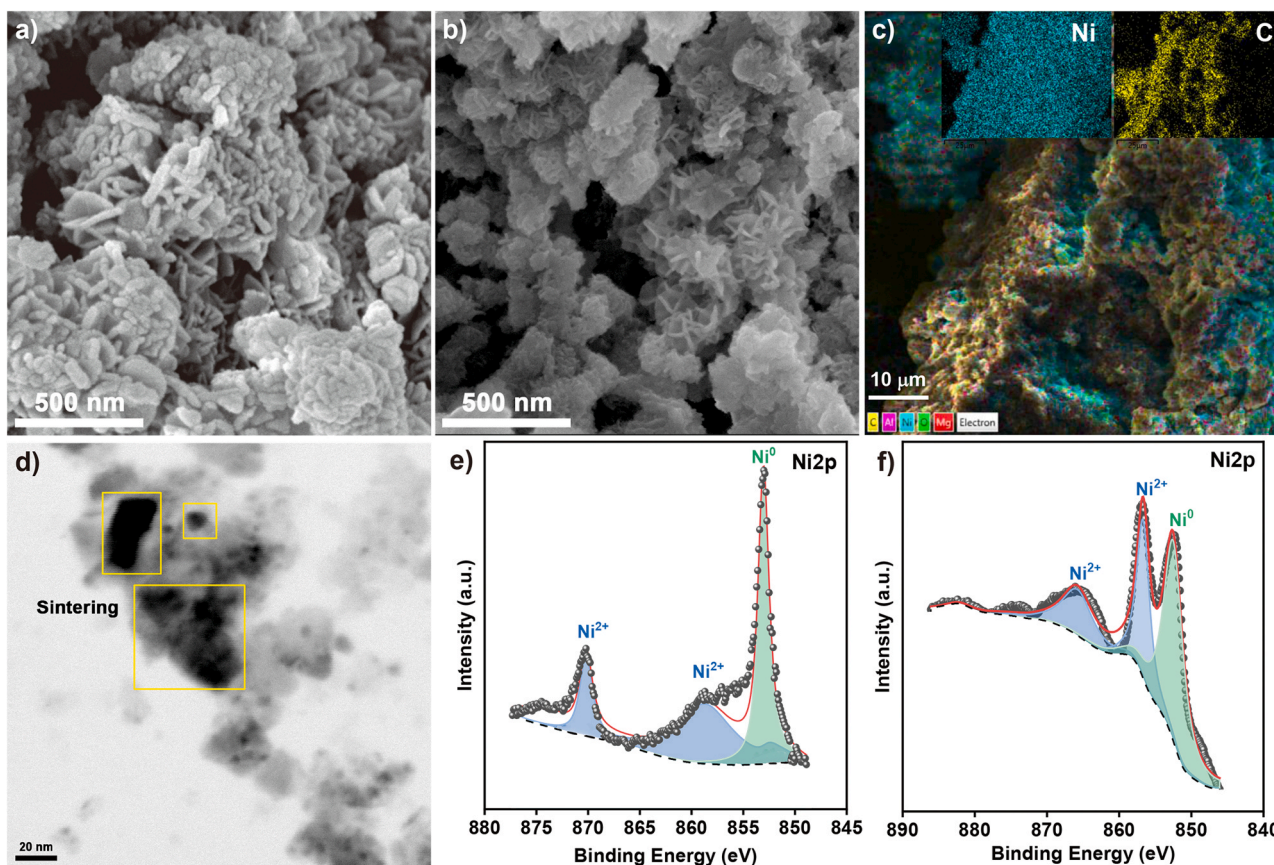

Fig. 11. SEM images of spent Ni/MAO-10 after 25 h SRT (without steam) (a) and after 30 h SRT (with steam) (b); EDX mapping of spent Ni/MAO-10 after 25 h SRT (c); TEM image of spent Ni/MAO-10 (d); Ni2p spectra of fresh (e) and spent Ni/MAO-10 after 30 h SRT (with steam) (f).

activity of Ni/MAO-10 should be due to the uncompleted coke elimination or slight oxidation of the metallic Ni. The toluene conversion was decreased by 18.3% compared with the initial experiment, and the syngas yield over Ni/MAO-10 was also reduced from 196.2 mmol/g-Ni to 163.2 mmol/g-Ni. As mentioned in previous literature, the steam introduction cannot completely remove carbon deposition, and the fibrous coke can be observed in many studies [44–46]. Similar trends can also be observed during the next three reforming experiments when SRT was carried out over Ni/MAO-10 catalyst. It should be observed that the catalytic activity of Ni/MAO-10 in SRT cannot be regenerated after again regeneration through introducing steam. The decreased performance of Ni/MAO-10 in the fourth running was observed compared to the second running, which proved that carbon deposition accumulated on the catalyst surface still existed, and Ni oxidation became more serious. The toluene conversion decreased to 87.9% and total gas yield only achieved 752.1 mmol/g-Ni, and the H_2/CO here was 2.9 over Ni/MAO-10 proved there have not enough active sites to absorb reactants and generating H_2. Through again intermittent steam treatment (fifth and sixth running), the activity of Ni/MAO-10 was further decreased. The syngas yield decreased by approximately 36.7% compared with the first toluene conversion (without steam) over fresh Ni/MAO-10 catalyst. The last SRT during 26–30 h additionally demonstrated the activity was not recovered through the introduction of steam, and then toluene conversion and syngas yield decreased to 81.7% and 643.4 mmol/g-Ni, respectively.

As presented in Fig. 11, the spent catalysts after 5 and 6 cycle experiments (with and without steam) were characterized by SEM, EDX mapping, XPS, and TEM-EDS. However, the SEM image of the spent Ni/MAO-10 catalyst under non-steam (Fig. 11a) condition showed the rosette-like morphology was partly packed with carbon deposition, meanwhile, the porous structure of Ni/MAO-10 was damaged, inducing decreased S_{BET} in spent Ni/MAO-10. Inconsistent with some studies in the literature [47,48], the particular catalyst morphology of Ni/MAO-10 led to the inhibition of the growth of fibrous carbon, and the excess carbon was inserted into the petal structure and abundant pores. In contrast, the rosette-like morphology and S_{BET} of spent Ni/MAO-10 were basically retained when the catalyst was used for 30 h TOS in SRT (Fig. 11b), indicating most of the carbon deposition was eliminated after the introduction of steam (S/C=2). It demonstrated that coke produced under an inert atmosphere cannot be removed in time through the water-gas reaction when steam was dynamically introduced into the system. The EDX mapping (Fig. 11c) of the spent catalysts after use for 30 h showed that carbon deposition was not serious and metallic Ni was still highly dispersed on the surface of the Ni/MAO-10. The elements distribution observed in EDX mapping for fresh Ni/MAO-10, spent Ni/MAO-10 (without steam), and spent Ni/MAO-10 (S/C=2) were provided in Figs. S5-S7 for comparison. The serious carbon deposition of the spent Ni/MAO (without steam) after 25 h SRT was observed, which is well consistent with the results of N_2 physisorption (S_{BET}: 97.9 m^2/g and 128.1 m^2/g for spent Ni/MAO-10 without and with steam atmosphere) and XRD. In addition, the Ni particle sintering was also observed in spent Ni/MAO-10 after 30 h SRT (see Fig. 11d). The line scanning of the particle was verified by EDX (Fig. S8, Supporting Information) and XPS, and the results revealed the Ni/MAO-10 was oxidized when treated it intermittent steam during 30 h SRT. As discussed in XRD and H_2-TPR analyses, fresh Ni/MAO-10 with the reduction degree of 92.3% possessed metallic Ni and oxidized Ni^{2+} (Fig. 11e). The Ni2p spectra of spent Ni/MAO-10 (Fig. 11f) further verified the oxidation of metallic Ni, and 856.4 eV in spectra was attributed to Ni^{2+}. Based on the discussion above, Ni oxidation and sintering were the main reason for catalyst deactivation during long-term SRT, while carbon deposition and structure damage should be responsible for Ni/MAO-10 catalyst deactivation under a non-steam atmosphere.

3.4. Structure-activity relationships and reforming mechanisms

In order to obtain reliable kinetic data for SRT over the designed Ni/MAO catalysts, the toluene conversion should be controlled at below 20% for all measurements [49]. In addition, kinetic investigations should be carried out in the absence of heat and mass transfer resistances. Literature has stated that the back mixing and fluid channeling could be excluded if the catalyst bed height/catalyst particle size ratio (H/S) is above 50 and an internal diameter of a reactor to catalyst particle size ratio (D/S) above 30 [30]. Thus, in this case, the used quartz reactor with 6 mm i.d. and catalyst size of 200 μm was chosen for the kinetic study here. Furthermore, the influence of external mass-transfer on SRT over the designed catalyst was eliminated by adjusting the gas flow rate and catalyst usage, while other conditions like toluene feeding rate and S/C ratio were maintained as the same. Finally, SRT over Ni/MAO catalysts was performed under conditions: reaction temperature 400 – 600 °C, sample weight 20 mg, S/C= 2, GHSV= 40000 h^{-1}. The apparent activation energies (E_a) were calculated from the Arrhenius equation ($k = Ae^{-Ea/RT}$, where k can be replaced by TOF). As exhibited in Fig. 12a, the Arrhenius plots of different Ni/MAO catalysts in SRT showed that the E_a values of Ni/MAO-9, Ni/MAO-10, Ni/MAO-E, and Ni/MAO-150 were calculated to be 38.2, 25.6, 32.4, and 41.1 kJ/mol, respectively. As shown in Table 2, the calculated E_a of Ni/MAO-10 had the lowest E_a and highest TOF value, and hence can exhibit higher catalytic performance in toluene conversion and gas production. In comparison with the literature, the E_a of commercial Ni/Al$_2$O$_3$ in SRT was closed to that reported by Tang et al. [50], but the E_a of all Ni/MAO is lower than these studies [6,30,51]. In general, the low E_a of the catalyst would exhibit higher activity for SRT, but the calculated E_a actually depend on reforming conditions. Thus, E_a of the toluene reforming is varied in a wide range from the literature [51–53]. Based on these, Ni/MAO-10 with tailored property and excellent performance was deserved to be further investigated.

The metal surface area (MSA) and Ni dispersion of the catalysts were calculated based on the CO uptake from the results of CO pulse chemisorption, and a stoichiometric factor of CO:Ni = 1 was used. The detailed results were presented in Table S2 of the Supporting Information. To clearly observe the structure-activity relationship, a clear linear correlation between physicochemical properties of catalyst and the catalytic performance in SRT was displayed in Figs. 12b and 12c. It was observed that Ni/MAO-10 with the highest basicity (1.56 mmol/g) possessed the highest performance for syngas production under current conditions (reforming temperature of 550 °C, GHSV of 5000 h^{-1}, and S/C of 2). On the contrary, Ni/MAO-150 with the lowest S_{BET}, worst Ni dispersion, especially lowest basicity (0.99 mmol/g$_{cat}$) here showed worse adsorption for toluene and CO_2 to produce syngas. The superior activity of Ni/MAO-10 in SRT could be attributed to the better MSIs, Ni dispersion, low NCS, and rosette-like morphology among these catalysts. In addition, the correlated relationship between MSA and TOF value over the four catalysts was concluded in Fig. 12c. The tailored morphology of Ni/MAO-10 showed an excellent platform for Ni loading, and highly dispersed Ni contributed large MSA (12.4 m^2/g), indicating more active sites will be available for toluene conversion and syngas production. Moreover, Ni/MAO-150 with a plate-like structure and low V_{pore} cannot accommodate more Ni particles and feasible MSA (7.0 m^2/g), which thus exhibited the lowest TOF value (2.00 h^{-1}) for reforming of toluene under optimized conditions.

To understand the mechanism of toluene reforming under with/without steam atmosphere, the in-situ DRIFTS measurement for Ni/MAO-10 was employed for observing the intermediate conversion during the reforming. As can be seen from Fig. 13a, two characteristic functional bands at 1300–1670 cm^{-1} and 2820–3170 cm^{-1} of toluene were clearly observed at 30 °C (room temperature), which could be attributed to the C=C stretching of the aromatic ring and C-H stretching of aromatic ring and methyl group [54]. With the temperature increase to 400 °C, the intensity of these two typical functional groups becomes
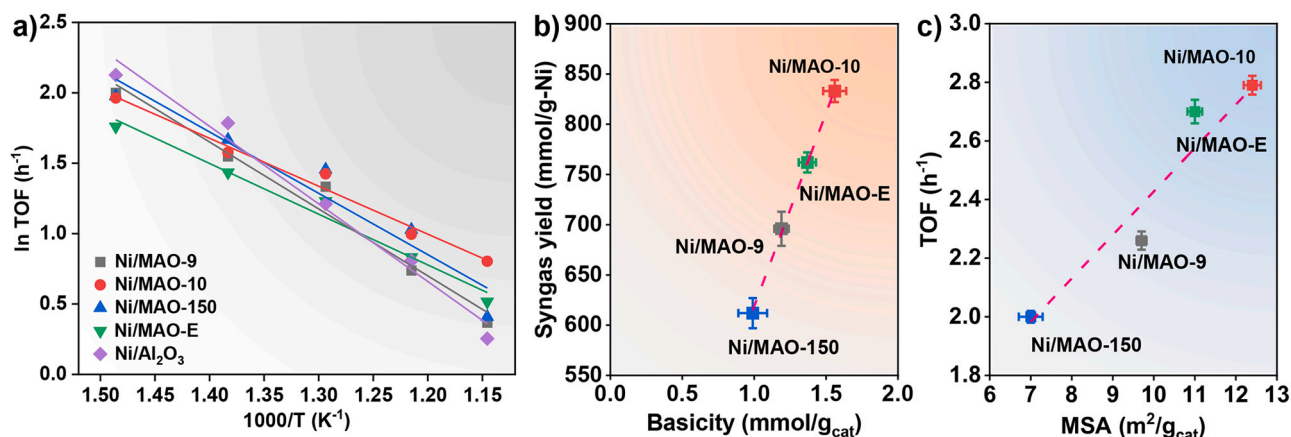
Fig. 12. Arrhenius plots for Ni/MAO catalysts in SRT (a); linear correlations between the basicity and syngas yield (b); linear correlations between the MSA and TOF (c).
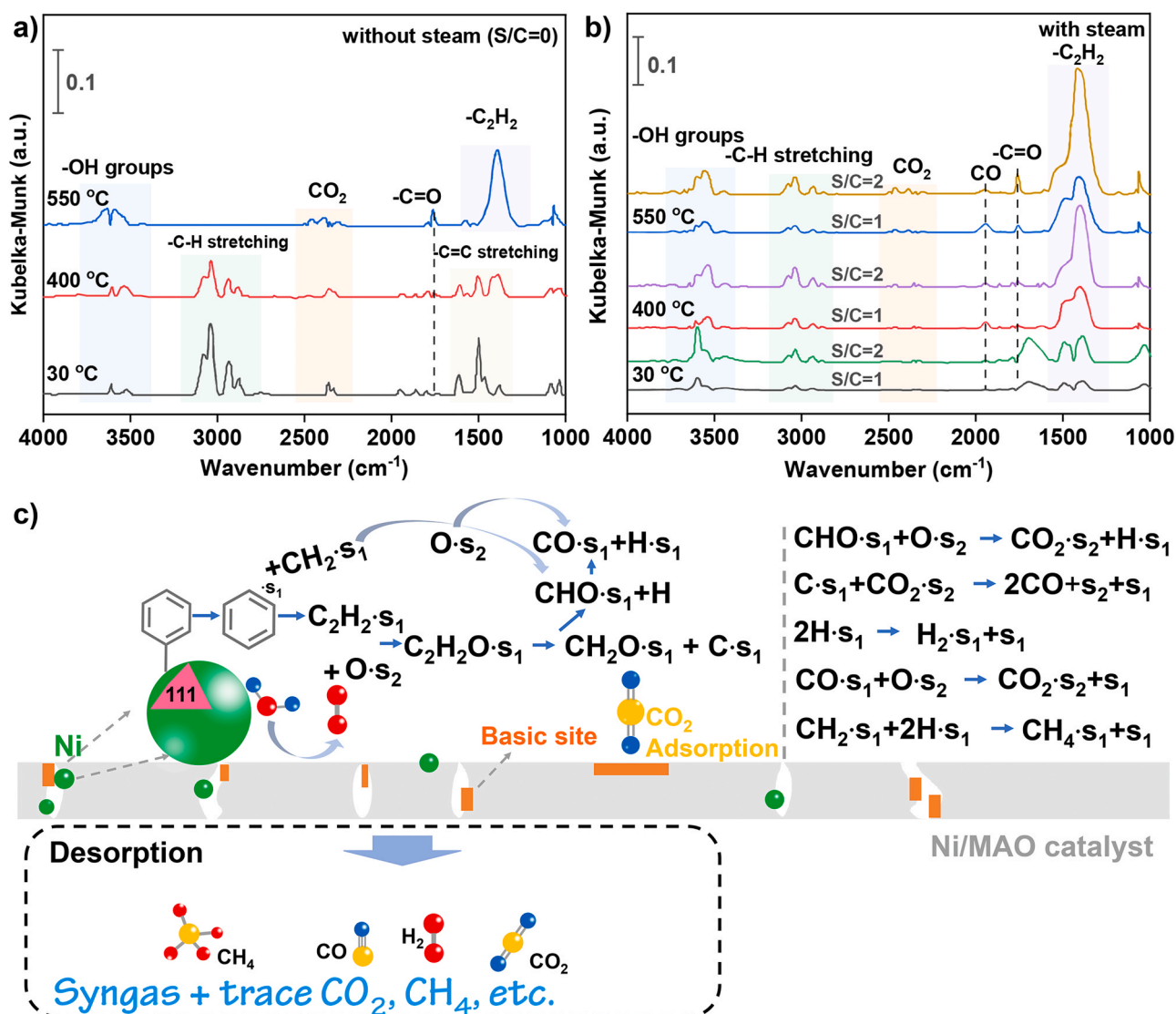

Fig. 13. In-situ DRIFTS experiments over Ni/MAO-10 under without (a) and with steam (b) atmospheres; Proposed mechanism for SRT under current conditions (c).

lower than at room temperature, which proved that the toluene was partly decomposed at 400 °C. Furthermore, the merged band at 1460 cm^{-1} assigned to C_2H_2 was observed based on the literature [55, 56]. However, the gaseous products such as CO, CH_4, and other intermediates cannot be found from the spectra, which proved the addition of steam is important to prove toluene cracking at low

temperatures. Therefore, in situ DRIFT experiment for SRT over Ni/MAO-10 catalyst was carried out to classify the pathway for syngas production. During the measurement, toluene and water were introduced continuously through bubbling to high-temperature in-situ cell. Fig. 13b shows the species changes on the surface of the Ni/MAO-10, and additional surface –OH groups centered at around 3450–3650 cm^{-1} are generated from steam introduction and basicity of the support. In addition to the C_2 species (i.e., C_2H_2), an important band at around 1760 cm^{-1} was observed which can be ascribed to –C═O stretching. The band at around 2820–3170 cm^{-1} together with –C═O stretching (at 1760 cm^{-1}) identified the existence of –CHO group, which can be a key intermediate to produce CO and H_2. The bands at 1944 cm^{-1} can be attributed to gaseous CO, and the higher CO peak at 500 °C proved the higher toluene conversion. To understand the influence of S/C ratio on the reaction pathway, the DRIFTS spectra for SRT under S/C= 1 were presented in Fig. 13b. In comparison with SRT under S/C= 2, the lower peak intensity observed at each temperature proved the lower toluene conversion and product yield. The less –OH under the lower S/C ratio revealed that –OH was not only from the basic site but also can be produced from water dissociation. Interestingly, more CO can be found when the S/C was 1, which demonstrated the water gas reaction and the reaction ($C_7H_8 + 7 H_2O → 7CO + 11 H_2$) were preferable under the conditions.

The proposed mechanism for SRT based on the above discussion is presented in Fig. 13c. Firstly, the steam is dissociated to active H and even produces H_2 and adsorbed O directly over Ni(111) plane at high temperature. Due to the basic properties of catalysts, the –OH group generated from water adsorption on the support surface can be dissociated to adsorbed H and adsorbed O. The adsorbed H free radicals can be terminated to obtain H_2 gas. Meanwhile, the adsorbed toluene can be cracked to adsorbed benzene and adsorbed methyl over the metallic site, and then adsorbed benzene could be further decomposed to -C_2H_2 species as we observed from in situ DRIFTS. After that, the adsorbed O species will react with adsorbed -C_2H_2 species or adsorbed CH_2 species to form adsorbed –CHO. It is noted that the –CHO formation from -C_2H_2 goes through –C_2H_2O and -CH_2O, and therefore generated carbon deposition. The carbon deposition can be further removed by Boudouard reaction and water-gas reaction (Eqs. 4–6) with CO_2 and steam. Subsequently, the adsorbed –CHO will be decomposed into CO and active H over the active site. Finally the further conversion of -CO, -CHO,–H, and -CH_2 will take place to produce adsorbed H_2, CO, CO_2, and CH_4, respectively.

In brief, it is suggested the SRT over the Ni/MAO catalysts to be structurally sensitive and enhanced syngas production depends on different factors such as basicity, reducibility, Ni dispersion, and S_{BET}. Moreover, the designed catalyst in this work could maintain the morphology of the special hydrotalcite-derived structure after calcination and reduction. Although the previous catalyst exhibited high toluene conversion at a lower temperature (i.e., 450 °C) due to the presence of bulk Ni on the catalyst surface, the Ni/MAO catalyst obtained here with the uniform Ni dispersion and therefore showed better stability under rigorous condition. In view of carbon deposition and Ni oxidation when SRT was performed under inert and steam atmosphere during long-term tests, the regeneration under air and hydrogen are proved to be commonly used in laboratory and industry. In addition, it is also possible to add other metals (e.g., transition and rare earth metal) into the system to further enhance the activity and stability of Ni/MAO catalysts for SRT [57–59].

4. Conclusions

In summary, we developed a series of Ni/MAO catalysts derived from Ni-Mg-Al hydrotalcites and successfully demonstrated the superior activity of them in toluene conversion at low temperature. The effects of temperatures and S/C ratios on the syngas yield and toluene conversion over the designed Ni/MAO catalysts were studied. The results suggested

that Ni/MAO-10 exhibited the highest toluene conversion (95.3%) and syngas production at 550 °C. The characterization results confirmed that Ni/MAO-10 possessed a rosette-like structure with large S_{BET} (131.2 m^2/g) that could provide larger space for Ni loading, and therefore enhance Ni dispersion and MSA, which can endure rigorous conditions. The intermittent supply of steam verified the stability of the Ni/MAO-10 catalyst, that is, stronger basicity (1.59 mmol/g$_{cat}$) of Ni/MAO-10 could adsorb generated CO_2 and react with deposited coke to produce CO. However, the unreacted CO_2 and additional steam could facilitate Ni oxidation. Therefore, Ni oxidation was the main reason for catalyst deactivation during long-term SRT rather than carbon deposition. Furthermore, the mechanism of the toluene reforming was identified by the in-situ DRIFTS, and the abundant Ni(111) plane provided excellent active sites for syngas production during reforming reaction. Based on the results we have, Ni/MAO catalysts have the potential to be used for the removal of real tar during biomass gasification.

CRediT authorship contribution statement

Jie Ren: Conceptualization, Methodology, Software, Formal analysis, Investigation, Writing – original, review & editing, Funding acquisition. **Yi-Ling Liu:** Investigation, Data curation, Resources, Writing - original draft.

Declaration of Competing Interest

The authors declare that they have no known competing financial interests or personal relationships that could have appeared to influence the work reported in this paper.

Acknowledgments

Appendix A. Supporting information

Supplementary data associated with this article can be found in the online version at doi:10.1016/j.apcatb.2021.120743.

References

[1] J. Ren, J.P. Cao, X.Y. Zhao, F.L. Yang, X.Y. Wei, Recent advances in syngas production from biomass catalytic gasification: a critical review on reactors, catalysts, catalytic mechanisms and mathematical models, Renew. Sustain. Energy Rev. 116 (2019) 109426–109451, https://doi.org/10.1016/j.rser.2019.109426.

[2] M. Patel, X. Zhang, A. Kumar, Techno-economic and life cycle assessment on lignocellulosic biomass thermochemical conversion technologies: a review, Renew. Sustain. Energy Rev. 53 (2016) 1486–1499, https://doi.org/10.1016/j.rser.2015.09.070.

[3] E. Shayan, V. Zare, I. Mirzaee, Hydrogen production from biomass gasification; a theoretical comparison of using different gasification agents, Energy Convers. Manag. 159 (2018) 30–41, https://doi.org/10.1016/j.enconman.2017.12.096.

[4] N. Gao, K. Chen, C. Quan, S. Wu, Nickel supported over MCM-41 coated ceramic membrane for steam reforming of real tar, Int. J. Hydrogen Energy 46 (2021) 20882–20892, https://doi.org/10.1016/j.ijhydene.2021.03.213.

[5] L. Han, Q. Liu, K. Lin, Q. Wang, N. Rong, X. Liang, A.R. Shaikh, Y. Feng, Y. Zhong, Enhanced hydrogen production via catalytic toluene reforming with in situ carbon dioxide capture: effects of a hybrid iron-calcium composite prepared by impregnation, Energy Convers. Manag. 214 (2020) 112834–112847, https://doi.org/10.1016/j.enconman.2020.112834.

[6] J. Ren, J.P. Cao, F.L. Yang, X.Y. Zhao, W. Tang, X. Cui, Q. Chen, X.Y. Wei, Layered uniformly delocalized electronic structure of carbon supported Ni catalyst for catalytic reforming of toluene and biomass tar, Energy Convers. Manag. 183 (2019) 182–192, https://doi.org/10.1016/j.enconman.2018.12.093.

[7] I. Zamboni, C. Courson, A. Kiennemann, Fe-Ca interactions in Fe-based/CaO catalyst/sorbent for CO_2 sorption and hydrogen production from toluene steam

reforming, Appl. Catal. B-Environ. 203 (2017) 154–165, https://doi.org/10.1016/j.apcatb.2016.10.024.

[8] N. Gao, J. Salisu, C. Quan, P. Williams, Modified nickel-based catalysts for improved steam reforming of biomass tar: a critical review, Renew. Sustain. Energy Rev. 145 (2021) 111023–111052, https://doi.org/10.1016/j.rser.2021.111023.

[9] Z.Y. Du, Z.H. Zhang, C. Xu, X.B. Wang, W.Y. Li, Low-temperature steam reforming of toluene and biomass tar over biochar-supported Ni nanoparticles, ACS Sustain. Chem. Eng. 7 (2019) 3111–3119, https://doi.org/10.1021/acssuschemeng.8b04872.

[10] C. Quan, H. Wang, N. Gao, Development of activated biochar supported Ni catalyst for enhancing toluene steam reforming, Int. J. Energy Res. 44 (2020) 5749–5764, https://doi.org/10.1002/er.5335.

[11] Z. Zhang, L. Liu, B. Shen, C. Wu, Preparation, modification and development of Ni-based catalysts for catalytic reforming of tar produced from biomass gasification, Renew. Sustain. Energy Rev. 94 (2018) 1086–1109, https://doi.org/10.1016/j.rser.2018.07.010.

[12] J. Ashok, N. Dewangan, S. Das, P. Hongmanorom, M.H. Wai, K. Tomishige, S. Kawi, Recent progress in the development of catalysts for steam reforming of biomass tar model reaction, Fuel Process. Technol. 199 (2020) 106252–106279, https://doi.org/10.1016/j.fuproc.2019.106252.

[13] T. Ahmed, S. Xiu, L. Wang, A. Shahbazi, Investigation of Ni/Fe/Mg zeolite-supported catalysts in steam reforming of tar using simulated-toluene as model compound, Fuel 211 (2018) 566–571, https://doi.org/10.1016/j.fuel.2017.09.051.

[14] U. Sikander, M.F. Samsudin, S. Sufian, K. KuShaari, C.F. Kait, S.R. Naqvi, W. H. Chen, Tailored hydrotalcite-based Mg-Ni-Al catalyst for hydrogen production via methane decomposition: Effect of nickel concentration and spinel-like structures, Int. J. Hydrogen Energy 44 (2019) 14424–14433, https://doi.org/10.1016/j.ijhydene.2018.10.224.

[15] F. Zhou, N. Pan, H. Chen, X. Xu, C. Wang, Y. Du, Y. Guo, Z. Zeng, L. Li, Hydrogen production through steam reforming of toluene over Ce, Zr or Fe promoted Ni-Mg-Al hydrotalcite-derived catalysts at low temperature, Energy Convers. Manag. 196 (2019) 677–687, https://doi.org/10.1016/j.enconman.2019.06.047.

[16] U. Sikander, S. Sufian, M.A. Salam, A review of hydrotalcite based catalysts for hydrogen production systems, Int. J. Hydrogen Energy 42 (2017) 19851–19868, https://doi.org/10.1016/j.ijhydene.2017.06.089.

[17] F.M. Josuinkas, C.P.B. Quitete, N.F.P. Ribeiro, M.M.V.M. Souza, Steam reforming of model gasification tar compounds over nickel catalysts prepared from hydrotalcite precursors, Fuel Process. Technol. 121 (2014) 76–82, https://doi.org/10.1016/j.fuproc.2014.01.007.

[18] J. Ren, F.L. Yang, Y.L. Liu, Enhanced H_2-rich gas production via steam reforming of toluene over Ni-based hydrotalcite-derived catalysts at low temperature, ACS Sustain. Chem. Eng. 9 (2021) 8315–8326, https://doi.org/10.1021/acssuschemeng.1c03122.

[19] K.S.W. Sing, Reporting physisorption data for gas/solid systems with special reference to the determination of surface area and porosity (Recommendations 1984), Pure Appl. Chem. 57 (1985) 603–619, https://doi.org/10.1351/pac198557040603.

[20] S. Abelló, J. Pérez-Ramírez, Steam activation of Mg–Al hydrotalcite. Influence on the properties of the derived mixed oxides, Micro Mesopor. Mat. 96 (2006) 102–108, https://doi.org/10.1016/j.micromeso.2006.06.018.

[21] C. Quan, N. Gao, H. Wang, H. Sun, C. Wu, X. Wang, Z. Ma, Ethanol steam reforming on Ni/CaO catalysts for coproduction of hydrogen and carbon nanotubes, Int. J. Energy Res. 43 (2019) 1255–1271, https://doi.org/10.1002/er.4365.

[22] H. Wang, W. Liu, Y. Wang, N. Tao, H. Cai, J. Liu, J. Lv, Mg–Al mixed oxide derived from hydrotalcites prepared using the solvent-free method: A stable acid–base bifunctional catalyst for continuous-flow transesterification of dimethyl carbonate and ethanol, Ind. Eng. Chem. Res. 59 (2020) 5591–5600, https://doi.org/10.1021/acs.iecr.9b06303.

[23] J. Ren, C. Mebrahtu, R. Palkovits, Ni-based catalysts supported on Mg–Al hydrotalcites with different morphologies for CO_2 methanation: exploring the effect of metal–support interaction, Catal. Sci. Technol. 10 (2020) 1902–1913, https://doi.org/10.1039/C9CY02523E.

[24] J. Ashok, S. Das, N. Dewangan, S. Kawi, H_2S and NO_x tolerance capability of CeO_2 doped $La_{1-x}Ce_xCo_{0.5}Ti_{0.5}O_{3-δ}$ perovskites for steam reforming of biomass tar model reaction, Energy Convers. Manag. X 1 (2019) 100003–100015, https://doi.org/10.1016/j.ecmx.2019.100003.

[25] Q. Wang, H.H. Tay, Z. Guo, L. Chen, Y. Liu, J. Chang, Z. Zhong, J. Luo, A. Borgna, Morphology and composition controllable synthesis of Mg–Al–CO_3 hydrotalcites by tuning the synthesis pH and the CO_2 capture capacity, Appl. Clay Sci. 55 (2012) 18–26, https://doi.org/10.1016/j.clay.2011.07.024.

[26] F. Besenbacher, M. Brorson, B.S. Clausen, S. Helveg, B. Hinnemann, J. Kibsgaard, J. V. Lauritsen, P.G. Moses, J.K. Nørskov, H. Topsøe, Recent STM, DFT and HAADF-STEM studies of sulfide-based hydrotreating catalysts: Insight into mechanistic, structural and particle size effects, Catal. Today 130 (2008) 86–96, https://doi.org/10.1016/j.cattod.2007.08.009.

[27] F.L. Yang, J.P. Cao, X.Y. Zhao, J. Ren, W. Tang, X. Huang, X.B. Feng, M. Zhao, X. Cui, X.Y. Wei, Acid washed lignite char supported bimetallic Ni-Co catalyst for low temperature catalytic reforming of corncob derived volatiles, Energy Convers. Manag. 196 (2019) 1257–1266, https://doi.org/10.1016/j.enconman.2019.06.075.

[28] K. Yuan, J.Q. Zhong, X. Zhou, L. Xu, S.L. Bergman, K. Wu, G.Q. Xu, S.L. Bernasek, H.X. Li, W. Chen, Dynamic oxygen on surface: catalytic intermediate and coking barrier in the modeled CO_2 reforming of CH_4 on Ni (111), ACS Catal. 6 (2016) 4330–4339, https://doi.org/10.1021/acscatal.6b00357.

[29] A. Jess, Mechanisms and kinetics of thermal reactions of aromatic hydrocarbons from pyrolysis of solid fuels, Fuel 75 (1996) 1441–1448, https://doi.org/10.1016/0016-2361(96)00136-6.

[30] X. Zou, T. Chen, P. Zhang, D. Chen, J. He, Y. Dang, Z. Ma, Y. Chen, P. Toloueinia, C. Zhu, J. Xie, H. Liu, S.L. Suib, High catalytic performance of Fe-Ni/Palygorskite in the steam reforming of toluene for hydrogen production, Appl. Energy 226 (2018) 827–837, https://doi.org/10.1016/j.apenergy.2018.06.005.

[31] T. Chen, H. Liu, P. Shi, D. Chen, L. Song, H. He, R.L. Frost, CO_2 reforming of toluene as model compound of biomass tar on Ni/Palygorskite, Fuel 107 (2013) 699–705, https://doi.org/10.1016/j.fuel.2012.12.036.

[32] N. Gao, M. Cheng, C. Quan, Y. Zheng, Syngas production via combined dry and steam reforming of methane over Ni-Ce/ZSM-5 catalyst, Fuel 273 (2020) 117702–117713, https://doi.org/10.1016/j.fuel.2020.117702.

[33] T.A. Le, M.S. Kim, S.H. Lee, T.W. Kim, E.D. Park, CO and CO_2 methanation over supported Ni catalysts, Catal. Today 293–294 (2017) 89–96, https://doi.org/10.1016/j.cattod.2016.12.036.

[34] L. Foppa, T. Margossian, S.M. Kim, C. Müller, C. Copéret, K. Larmier, A. Comas-Vives, Contrasting the role of Ni/Al_2O_3 interfaces in water–gas shift and dry reforming of methane, J. Am. Chem. Soc. 139 (2017) 17128–17139, https://doi.org/10.1021/jacs.7b08984.

[35] P. Cao, H. Zhao, S. Adegbite, B. Yang, E. Lester, T. Wu, Stabilized CO_2 reforming of CH_4 on modified Ni/Al_2O_3 catalysts via in-situ K_2CO_3-enabled dynamic coke elimination reaction, Fuel 298 (2021) 120599–120608, https://doi.org/10.1016/j.fuel.2021.120599.

[36] J. Ren, Y.L. Liu, X.Y. Zhao, J.P. Cao, Methanation of syngas from biomass gasification: an overview, Int. J. Hydrogen Energy 45 (2020) 4223–4243, https://doi.org/10.1016/j.ijhydene.2019.12.023.

[37] F. Jiao, J. Li, X. Pan, J. Xiao, H. Li, H. Ma, M. Wei, Y. Pan, Z. Zhou, M. Li, S. Miao, J. Li, Y. Zhu, D. Xiao, T. He, J. Yang, F. Qi, Q. Fu, X. Bao, Selective conversion of syngas to light olefins, Science 351 (2016) 1065–1068, https://doi.org/10.1126/science.aaf1835.

[38] S.R. Foit, I.C. Vinke, L.G.J. deHaart, R.-A. Eichel, Power-to-syngas: an enabling technology for the transition of the energy system? Angew. Chem. Int. Ed. 56 (2017) 5402–5411, https://doi.org/10.1002/anie.201607552.

[39] M. Artetxe, J. Alvarez, M.A. Nahil, M. Olazar, P.T. Williams, Steam reforming of different biomass tar model compounds over Ni/Al_2O_3 catalysts, Energy Convers. Manag. 136 (2017) 119–126, https://doi.org/10.1016/j.enconman.2016.12.092.

[40] J.P. Cao, J. Ren, X.Y. Zhao, X.Y. Wei, T. Takarada, Effect of atmosphere on carbon deposition of Ni/Al_2O_3 and Ni-loaded on lignite char during reforming of toluene as a biomass tar model compound, Fuel 217 (2018) 515–521, https://doi.org/10.1016/j.fuel.2017.12.121.

[41] L. Santamaria, A. Arregi, G. Lopez, M. Artetxe, M. Amutio, J. Bilbao, M. Olazar, Effect of La_2O_3 promotion on a Ni/Al_2O_3 catalyst for H_2 production in the in-line biomass pyrolysis-reforming, Fuel 262 (2020) 116593–116605, https://doi.org/10.1016/j.fuel.2019.116593.

[42] D. Świerczyński, S. Libs, C. Courson, A. Kiennemann, Steam reforming of tar from a biomass gasification process over Ni/olivine catalyst using toluene as a model compound, Appl. Catal. B-Environ. 74 (2007) 211–222, https://doi.org/10.1016/j.apcatb.2007.01.017.

[43] N. Gao, S. Liu, Y. Han, C. Xing, A. Li, Steam reforming of biomass tar for hydrogen production over NiO/ceramic foam catalyst, Int. J. Hydrogen Energy 40 (2015) 7983–7990, https://doi.org/10.1016/j.ijhydene.2015.04.050.

[44] L. He, S. Hu, L. Jiang, S.S.A. Syed-Hassan, Y. Wang, K. Xu, S. Su, J. Xiang, L. Xiao, H. Chi, X. Chen, Opposite effects of self-growth amorphous carbon and carbon nanotubes on the reforming of toluene with Ni/α-Al_2O_3 for hydrogen production, Int. J. Hydrogen Energy 42 (2017) 14439–14448, https://doi.org/10.1016/j.ijhydene.2017.04.230.

[45] U. Oemar, P.S. Ang, K. Hidajat, S. Kawi, Promotional effect of Fe on perovskite $LaNi_xFe_{1-x}O_3$ catalyst for hydrogen production via steam reforming of toluene, Int. J. Hydrogen Energy 38 (2013) 5525–5534, https://doi.org/10.1016/j.ijhydene.2013.02.083.

[46] N.K. Park, Y.J. Lee, B.C. Kwon, T.J. Lee, S.H. Kang, B.U. Hong, T. Kim, Optimization of nickel-based catalyst composition and reaction conditions for the prevention of carbon deposition in toluene reforming, Energies 12 (2019) 1307–1320, https://doi.org/10.3390/en12071307.

[47] Z. Zhang, T. Wei, G. Chen, C. Li, D. Dong, W. Wu, Q. Liu, X. Hu, Understanding correlation of the interaction between nickel and alumina with the catalytic behaviors in steam reforming and methanation, Fuel 250 (2019) 176–193, https://doi.org/10.1016/j.fuel.2019.04.005.

[48] A. Ochoa, J. Bilbao, A.G. Gayubo, P. Castaño, Coke formation and deactivation during catalytic reforming of biomass and waste pyrolysis products: a review, Renew. Sustain. Energy Rev. 119 (2020) 109600–109629, https://doi.org/10.1016/j.rser.2019.109600.

[49] U. Oemar, A. Ming Li, K. Hidajat, S. Kawi, Mechanism and kinetic modeling for steam reforming of toluene on $La_{0.8}Sr_{0.2}Ni_{0.8}Fe_{0.2}O_3$ catalyst, AIChE J. 60 (2014) 4190–4198, https://doi.org/10.1002/aic.14573.

[50] W. Tang, J.P. Cao, F.L. Yang, X.B. Feng, J. Ren, J.X. Wang, X.Y. Zhao, M. Zhao, X. Cui, X.Y. Wei, Highly active and stable HF acid modified HZSM-5 supported Ni catalysts for steam reforming of toluene and biomass pyrolysis tar, Energy Convers. Manag. 212 (2020) 112799–112811, https://doi.org/10.1016/j.enconman.2020.112799.

[51] D. Mukai, S. Tochiya, Y. Murai, M. Imori, Y. Sugiura, Y. Sekine, Structure and activity of Ni/$La_{0.7}Sr_{0.3}AlO_{3-δ}$ catalyst for hydrogen production by steam reforming of toluene, Appl. Catal. A-Gen. 464–465 (2013) 78–86, https://doi.org/10.1016/j.apcata.2013.05.023.

[52] K. Takise, T. Higo, D. Mukai, S. Ogo, Y. Sugiura, Y. Sekine, Highly active and stable Co/La$_{0.7}$Sr$_{0.3}$AlO$_{3-\delta}$ catalyst for steam reforming of toluene, Catal. Today 265 (2016) 111–117, https://doi.org/10.1016/j.cattod.2015.08.059.

[53] S. Yamaguchi, T. Ozaki, T. Suyama, H. Muroyama, T. Matsui, K. Eguchi, Evaluation of regenerative function and activity of reforming toluene by composite catalyst containing spinel oxide, Int. J. Hydrogen Energy 44 (2019) 9338–9347, https://doi.org/10.1016/j.ijhydene.2019.02.101.

[54] S. Sun, F. Zhang, Z. Qi, J. Ding, J. Bao, C. Gao, Rapid discovery of a photocatalyst for air purification by high-throughput screening, ChemCatChem 6 (2014) 2535–2539, https://doi.org/10.1002/cctc.201402332.

[55] D. Mukai, Y. Murai, T. Higo, S. Tochiya, T. Hashimoto, Y. Sugiura, Y. Sekine, In situ IR study for elucidating reaction mechanism of toluene steam reforming over Ni/La$_{0.7}$Sr$_{0.3}$AlO$_{3-\delta}$ catalyst, Appl. Catal. A-Gen. 466 (2013) 190–197, https://doi.org/10.1016/j.apcata.2013.06.052.

[56] M. Derudi, D. Polino, C. Cavallotti, Toluene and benzyl decomposition mechanisms: elementary reactions and kinetic simulations, Phys. Chem. 13 (2011) 21308–21318, https://doi.org/10.1039/C1CP22601K.

[57] S. Jayaprakash, N. Dewangan, A. Jangam, S. Kawi, H$_2$S-resistant CeO$_2$-NiO-MgO-Al$_2$O$_3$ LDH-derived catalysts for steam reforming of toluene, Fuel Process. Technol. 219 (2021) 106871–106882, https://doi.org/10.1016/j.fuproc.2021.106871.

[58] G. Mitran, D.G. Mieritz, D.K. Seo, Hydrotalcites with vanadium, effective catalysts for steam reforming of toluene, Int. J. Hydrogen Energy 42 (2017) 21732–21740, https://doi.org/10.1016/j.ijhydene.2017.07.097.

[59] S. Zhou, Z. Chen, H. Gong, X. Wang, T. Zhu, Y. Zhou, Low-temperature catalytic steam reforming of toluene as a biomass tar model compound over three-dimensional ordered macroporous Ni-Pt/Ce$_{1-x}$Zr$_x$O$_2$ catalysts, Appl. Catal. A-Gen. 607 (2020) 117859–117871, https://doi.org/10.1016/j.apcata.2020.117859.